

# **Colloids and Gels Containing Magnetic Nanoparticles**

by

Lelin Zheng

A thesis submitted in partial fulfillment of the requirements for the degree of

Master of Science

in

**MATERIALS ENGINEERING**

Department of Chemical and Materials Engineering  
University of Alberta

© Lelin Zheng, 2019

## **Abstract**

Magnetic nanoparticles (MNPs), whose positions and motions can be controlled by external magnetic fields, have been widely used and designed into applications both in academia and industries especially when dispersed in media such as colloids and hydrogels, owing to the combination of their unique properties and the advantages of the media. These applications include drug delivery, contamination treatment, photonic crystal e-paper, and soft actuators. In recent years, there has been rapid advances in these fields.

This thesis summarizes two projects. In the first project, a colorimetric voltmeter has been fabricated using magnetic  $\text{Fe}_3\text{O}_4@\text{SiO}_2$  nanoparticles in colloids for the application as an overpotential alarm system in zinc-air batteries. These colloidal nanoparticles self-assemble into an amorphous photonic crystal whose interparticle distance varies under electric field, leading to a colorimetric display of the applied field. By connecting the two electrodes of zinc-air battery to each end of a capacitor filled with the two colloidal nanoparticles between transparent electrodes, I have achieved a simple and intuitive way to monitor the status of rechargeable batteries. Specifically, the performance of zinc-air battery, including discharging, charging, overcharging and aging behaviors have been monitored by the colour display of the capacitor device. In general, the application of colloidal MNPs as a battery monitoring device are proposed and discussed.

In the second project, I have reviewed the recent progress in the field of magnetic hydrogels, especially in soft robotics applications. Firstly, the strategies for dispersing the MNPs in the hydrogels are discussed with examples from the literature. Secondly, the three major fields of current applications, including drug delivery, enzyme immobilization and separation of cell and

protein, as well as microorganisms and organics detection and purification of wastewater are reviewed. Thirdly, the operation principles and application of magnetic hydrogels in the upcoming field of soft robotics are demonstrated with examples.

Overall, this thesis describes various aspects of MNP study, ranging from synthesis to applications in colloidal suspension and in hydrogel media. I harnessed amorphous photonic crystal property of colloidal MNP to fabricate a colorimetric voltmeter that monitors the overcharging status of zinc-air battery. I reviewed the dispersion and application of MNPs in hydrogels, with an emphasis on the applications in soft robotics systems. I anticipate that my work can inspire novel application-driven researches on MNP based materials. Specifically, I envision applications of MNP based colloids and gels in soft devices such as battery indicators, biomimicking artificial muscles and sensory artificial skins.

**Key words:** magnetic nanoparticles,  $\text{Fe}_3\text{O}_4$  nanoparticles, colloids, amorphous photonic crystals, magnetic hydrogels

# Preface

(Mandatory due to collaborative work)

This thesis is organized in five chapters.

Chapter 1 is the introduction, which focuses on the basic property of magnetic nanoparticles itself as well as in media including colloids and hydrogels. The fabrication methods and applications field of magnetic nanoparticles were also reviewed.

Chapter 2 is the background, which emphasizes on magnetic nanoparticles behaviors under electric field and the introduction of amorphous crystal structure.

Chapter 3 of this thesis has been submitted to *ACS Applied Nano Materials* as L. Zheng, T. Tran, D. Zhalmuratova, H.-J. Chung, “Colorimetric Voltmeter Using Colloidal  $\text{Fe}_3\text{O}_4@/\text{SiO}_2$  Nanoparticles as an Overpotential Alarm System for Zinc-air Battery”. L. Zheng conceived the idea, performed the experiments, and carried out data interpretation. T. Tran and D. Zhalmuratova helped with characterization and fabrication of the zinc-air battery part. H.-J. Chung provided guidance throughout the experiments and revised the manuscript.

Chapter 4 of this thesis will be further refined and be prepared for a journal submission as a review paper focusing on magnetic hydrogels and elastomers. This chapter will comprise a part of the review paper.

The overall conclusions of the thesis are summarized in Chapter 5.

## **Acknowledgements**

I express my sincere gratitude wholeheartedly to my supervisor, Dr. Hyun-Joong Chung for his continuous care, enduring support, and kind encouragement during my master study at the University of Alberta. He has always inspired me with his enthusiasm and dedication for research. I deeply appreciate all his advice and supports to make my MSc experience at University of Alberta. I am also very grateful for his patience, inspiration and immerse knowledge in the areas of expertise.

I was fortunate to have great groupmates during my master's study at the University of Alberta. They made my two years of life in Canada fulfilling and they helped me a lot in both academic fields and life. I am especially appreciative of Wendy Tran, Dinara Zhalmuratova, Hemant Charaya, Rosmi Abraham and Shide Qiu. Thanks for the help in doing research and above all for precious friendship.

I wish to express my great love and gratitude to my beloved family: To my mother, Suijie Liu, and my father, Chuanghong Zheng, for their endless love, unconditional support, encouragement, and always being there for me.

I would also like to convey thanks to every individual who helped in the realization of this thesis, and thanks for everyone I met in Canada.

Lelin Zheng

August 2019

# Table of Contents

<b>Abstract</b> .....	<b>ii</b>
<b>Preface</b> .....	<b>iv</b>
<b>Acknowledgements</b> .....	<b>v</b>
<b>Chapter 1. Introduction</b> .....	<b>1</b>
<i>1.1 Basic Properties of Magnetic Nanoparticles</i> .....	1
<i>1.2 Magnetic Nanoparticles in Colloids and Hydrogel</i> .....	3
<i>1.3 Fabrication Methods of Fe<sub>3</sub>O<sub>4</sub> Nanoparticles</i> .....	5
1.3.1 Solvothermal Method.....	5
1.3.2 Precipitation Method.....	6
1.3.3 Microemulsion Method .....	7
1.3.4 Sol-gel Method.....	7
1.3.5 Thermal Decomposition Method .....	8
<i>1.4 Application of Magnetic Nanoparticles</i> .....	8
1.4.1 Contamination Treatment.....	8
1.4.2 Biomedicine .....	9
1.4.3 Other Applications .....	10
<i>1.5 Scope of Thesis</i> .....	10
<b>Chapter 2. Background</b> .....	<b>13</b>
<i>2.1 Magnetic Nanoparticles under Electric Field</i> .....	13
2.1.1 Dispersing Nanoparticles in Colloidal Suspension .....	13
2.1.2 Nanoparticle under Electrophoresis .....	15
2.1.3 Self-Assembly of Nanoparticles under Electrophoresis.....	16
<i>2.2 Amorphous Photonic Crystal</i> .....	18
2.2.1 Structural Colour .....	18

2.2.2 Photonic Crystal .....	20
2.2.3 Amorphous Photonic Crystal .....	23

### **Chapter 3. Colorimetric Voltmeter Using Colloidal Fe<sub>3</sub>O<sub>4</sub>@SiO<sub>2</sub> Nanoparticles as an Overpotential Alarm System for Zinc-air**

#### **Battery .....28**

<i>3.1 Introduction</i> .....	28
<i>3.2 Materials</i> .....	31
<i>3.3 Methods</i> .....	31
3.3.1 Experimental Methods .....	31
3.3.2 Characterization Methods .....	36
<i>3.4 Results and Discussion</i> .....	36
3.4.1 Material Characterization .....	36
3.4.2 Voltmeter Device Application .....	38
<i>3.5 Conclusion</i> .....	43

#### **Chapter 4. Recent Progress in Magnetic Hydrogels .....45**

<i>4.1 Strategies to Disperse Magnetic Nanoparticles in Hydrogels</i> .....	45
4.1.1 Blending Method .....	46
4.1.2 In situ Precipitation Method .....	48
4.1.3 Grafting-onto Method .....	48
<i>4.2 Traditional Applications of Magnetic Hydrogels</i> .....	50
4.2.1 Drug Delivery .....	50
4.2.2 Enzyme Immobilization, Cell and Protein Separation .....	52
4.2.3 Detection and Purification of Microorganisms and Organics in Wastewater .....	52
4.2.4 Magnetic Induced Actuation in Magnetic Hydrogels: From Small-scale Traditional Applications to Large-scale Soft Robotics .....	53
<i>4.3 Magnetic Hydrogels in Soft Robotics</i> .....	53

4.3.1 Introduction of Magnetic Hydrogels in Soft Robotics .....	53
4.3.2 Discussions on different types of magnetic hydrogels mechanism and the future trend .....	54
4.3.3 Magnetic Actuation in Hydrogels Verses Other Actuation Methods .....	59
<b>Chapter 5. Conclusion .....</b>	<b>65</b>
<b>Reference .....</b>	<b>69</b>

## List of Figures

Figure 1. Illustration of the magnetic dipoles arrangements for five types of magnetic materials with and without the external magnetic field (H). Reproduced with permission from [22].	2
Figure 2. (a) The dependence of magnetic coercivity on the nanoparticle size. The solid curve in the single domain regime is for noninteracting particles, while the dashed curve is for the particles that has coupling between them. Reproduced with permission from [24]. (b) Threshold spherical particle diameters for both maximum monodomain size( $d_{cr}$ ) and superparamagnetism( $d_{sp}$ ) . Reproduced with permission from [25].	3
Figure 3. The property and peculiarity of MNPs in both colloids and in hydrogels.	5
Figure 4. A summary diagram of the topics that are covered in this thesis. For the topic of colloidal MNPs, I developed a colorimetric voltmeter device by utilizing the electric field-modulated self-assembly of amorphous photonic crystal structure. For the topic of magnetic hydrogels, I reviewed the strategies of dispersing nanoparticles into hydrogel, followed by their applications with an emphasis on the emerging area of soft robotics.	12
Figure 5. (a) Schematic illustration that displays uncharged nanoparticles' tendency to collide and coalescence in the favor of energy. (b) Nanoparticles can be stabilized in an aqueous medium when they have surface charge. The ions in the double layers can protect the nanoparticles from aggregation. (c) Schematic illustrating the Diffuse Double Layer structure. (d) The dependence of the net interaction energy on the particle distance, which is the combination of repulsive and attractive energy. Reproduced with permission from [53].	14
Figure 6. Schematic illustration of the self-assembly of colloidal nanoparticles under electrical field. Reproduced with permission from [63].	18
Figure 7. Examples of 1-D, 2-D, 3-D photonic crystals. Different colors represents materials with different dielectric constants. Reproduced with permission from [80].	21

Figure 8. Colors of colloidal 1-D chain-like photonic crystal tuned by the external magnetic field and the reflectance spectrum results with peaks ranging from 450nm to 750nm. Reproduced with permission from [14].	23
Figure 9. SEM photos of amorphous crystal structures in different birds' feathers. Reproduced with permission from [77].	25
Figure 10. (a) PDOS of the RCP structure as a function of reduced frequency $d/\lambda$ . Two dips are shown where pseudogaps are located. Reproduced with permission from [90]. (b) The transition from pseudogap to PBG with increasing the refractive index contrast of the materials. Reproduced with permission from [93].	26
Figure 11. (a) A schematics of synthesis procedure of Fe <sub>3</sub> O <sub>4</sub> @SiO <sub>2</sub> nanoparticles. (b) Schematic illustration of the working mechanism of our colloidal amorphous photonic crystals (APCs) as a battery performance indicator.	33
Figure 12. (a) Zinc-Air battery working principle and reactions on each electrodes. Reproduced with permission from [124]. (b) Battery Encapsulation Acrylic Mold Specification.	34
Figure 13. (a) SEM image of Fe <sub>3</sub> O <sub>4</sub> (above) and Fe <sub>3</sub> O <sub>4</sub> @SiO <sub>2</sub> nanoparticles (below). Comparisons of (b) zeta-potential, (c) Dynamic light scattering results, and (d) XRD patterns of Fe <sub>3</sub> O <sub>4</sub> and Fe <sub>3</sub> O <sub>4</sub> @SiO <sub>2</sub> .	38
Figure 14. (a) Colorimetric displays of the colloidal APC device under various voltages. (b) Hue-Voltage calibration curve of nanoparticle device. (c) Schematic Illustration of the angle-dependence measurement. (d) Angle dependence on hue of the nanoparticle device's colour display.	39
Figure 15. (a) (left) Schematic illustration of battery and the APC device configurations and (right) the image of the actual battery and device. (b) Charge-discharge curves with overcharging, aging situations with colorimetric indication by the colloidal APC device. (c) Charge-discharge curves for battery without (red) and with (black) the colloidal APC device attached.	42

Figure 16. Strategies to disperse MNPs in hydrogels: (a) blending method; (b) in-situ precipitation method; (c) grafting-onto method. Reproduced with permission from [138]. ..... 46

Figure 17. Controlled drug release by magnetic hydrogels. (a) Mechanism 1: Pore closure upon the presence of oscillating magnetic field Reproduced with permission from [146]. (b) Mechanism 2: Pores open with the presence of magnetic field controlled by the phase transition of hydrogels. Reproduced with permission from [148]. ..... 52

Figure 18. (a) Bending experiment of magnetic hydrogel. Reproduced with permission from [156]. (b) Bending process of magnetic hydrogel with different nanoparticles content under the magnetic field. Reproduced with permission from [30]. (c) Highly flexible metallic cobalt hydrogels under compression. Reproduced with permission from [157]. ..... 56

## List of Tables

Table 1. List of Studies of Different Actuation Methods of Hydrogels.....	60
---	----

# Chapter 1. Introduction

Magnetic nanoparticles (MNPs) have been attracting an increasing interest in recent decades for their unique property and board range of applications, such as biomedicine[1, 2], magnetic resonance imaging[3, 4], drug delivery and tissue targeting[5-7], environmental remediation[8-10], microfluids[11], defect sensor[12], colloidal photonic crystal[13-15], and e-ink display system[16, 17]. Researches on the basic properties have revealed that MNPs have fundamentally distinctive properties compared to bulk magnetic materials, such as superparamagnetism, high coercivity, relatively low Curie temperature ( $T_c$ ), and high maximum saturation magnetization[18, 19]. MNPs can be prepared using Fe, Mn, Co and their oxides and alloys, among which the iron(II,III) oxide ( $Fe_3O_4$ ) are the most popular choice due to simple fabrication procedures and their biocompatibility (noncytotoxicity, capability of performing desired functions in the host) [20, 21] for application developments.

## 1.1 Basic Properties of Magnetic Nanoparticles

The magnetic property comes from the orbital magnetic moment and spin magnetic moment of electrons. For transition metal like Fe, Co, Ni, the magnetic moment of the atom comes from the incomplete 3d electron shell. The attraction and repulsion of magnetic materials is a result of its magnetic dipole. Based on the dipole arrangements of the material with or without the presence of applied magnetic field, it can be classified into five divisions, which are diamagnetic, paramagnetic, ferromagnetic, ferrimagnetic and antiferromagnetic materials demonstrated in Figure 1[22]. For ferromagnetic materials, the dipoles will be aligned in one direction with a

long-ranged order whether the applied magnetic field is presented or not. Therefore, there is a permanent moment exhibited macroscopically.

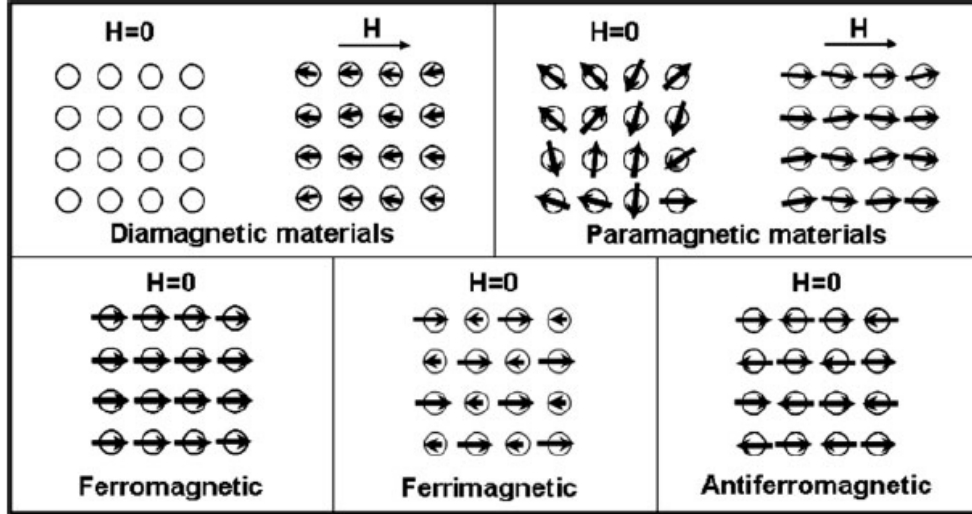


Figure 1. Illustration of the magnetic dipoles arrangements for five types of magnetic materials with and without the external magnetic field ( $H$ ). Reproduced with permission from [22].

For nano-sized magnetic particles, different properties from bulk material are observed and further investigated as a result of small size effects and surface effects. When the size of the ferromagnetic material decreases to a certain size  $r_c$ , the magnet will transform from the bulk state with multiple domains to a single domain state. It can be estimated by using the following equation[23]:

$$r_c = \left( \frac{6k_B T}{K_u} \right)^{\frac{1}{3}}$$

where  $T$  is temperature,  $k_B$  is Boltzmann constant, and  $K_u$  is the crystalline magnetoanisotropy.

If the size of the magnet keeps decreasing until it reaches the lower limit of single domain region  $r_0$ , where thermal energy is enough to overcome the energy barrier of magnetoanisotropy of the dipoles, the magnetic dipoles can be randomized in a very short period of time[24]. Particles in this regime do not have permanent magnetic moments like the one in bulk ferromagnetic materials but can respond to an external field and reach the saturation of moment easily. Upon removal of the external field, the magnetization of the nanoparticle will become zero (both the remnant magnetization  $M_r$  and the coercivity  $H_c$ ). This property of magnetic nanoparticle is referred as Superparamagnetism. Typically for  $\text{Fe}_3\text{O}_4$ , the critical diameter  $2r_c$  ( $d_{cr}$ ) is around 85 nm, and the threshold diameter for superparamagnetism is about 25 nm[25].

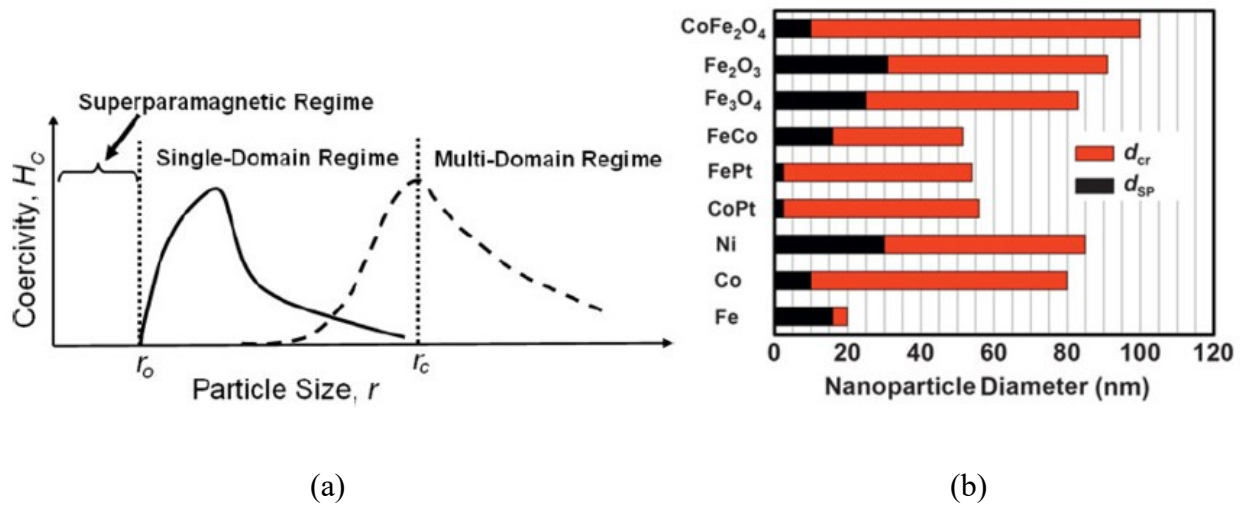


Figure 2. (a) The dependence of magnetic coercivity on the nanoparticle size. The solid curve in the single domain regime is for noninteracting particles, while the dashed curve is for the particles that has coupling between them. Reproduced with permission from [24]. (b) Threshold spherical particle diameters for both maximum monodomain size( $d_{cr}$ ) and superparamagnetism( $d_{sp}$ ) . Reproduced with permission from [25].

## 1.2 Magnetic Nanoparticles in Colloids and Hydrogel

MNPs are commonly dispersed in another medium to produce a composite that combine the advantages of magnetic responsiveness from the particles and the mechanical property of the media. MNP composites with colloids, gels, and elastomers are used in many practical applications.

Colloidal MNPs, or magnetic fluids, have attracted great research interest for having normal liquid behaviour while the fluid movement can be directed with magnetic particles dispersed inside. External magnetic field controls the flow of the colloid, as well as other properties; this system is uniquely useful for many applications.[26] Heat transfer, magnetic sealing, separation of liquids are the examples that have been widely used in industries[27-29]. When dispersed in the fluid, MNPs can also tailor the viscosity, surface tension, vapor pressure and other properties of the fluid. Moreover, MNPs induced by external fields can be self-assembled in the liquid into periodic structure, which are the mechanism behind many applications in display devices.

Magnetic hydrogel is an inorganic-organic nanocomposite. With magnetic nanoparticle embedded, it can react to the external magnetic field mechanically, or being actuated by tuning the field. Due to biocompatibility or even biodegradability of the hydrogels, such system has found many uses in biomedical fields such as drug delivery. Hydrogel has strong advantages in terms of high elasticity and stretchability, while the double network hydrogels can provide the toughness and robustness as a device.[30] When combining with functional hydrogels that self-healing, thermosensitive, pH sensitive or reactive to other stimuli, the magnetic hydrogel can be developed into multifunctional applications. In addition, recently developed technique for hydrogels such as injet printing could be applied in this field as well, opening more possibilities for applications. Overall, hydrogels are an ideal medium to disperse MNPs which provide both mechanical support and functionalities.

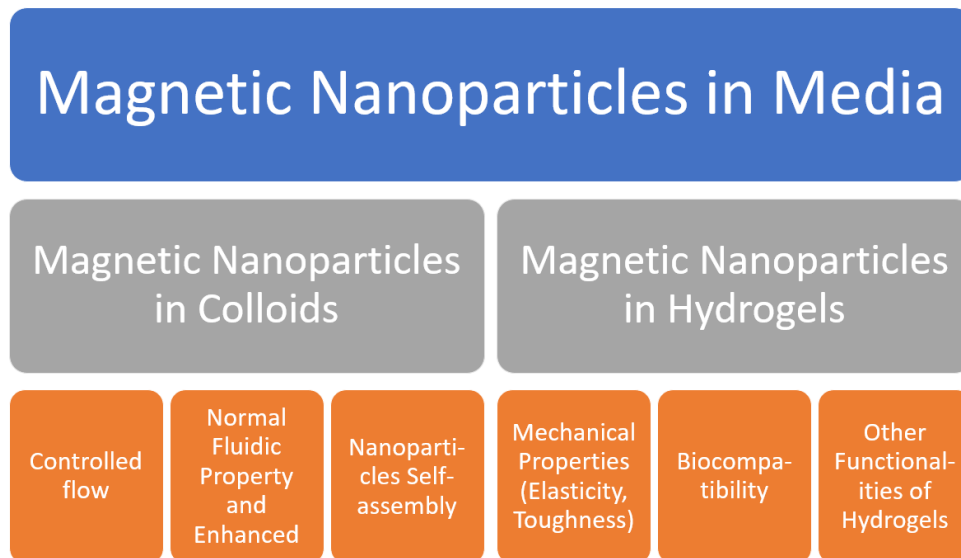


Figure 3. The property and peculiarity of MNPs in both colloids and in hydrogels.

### 1.3 Fabrication Methods of Fe<sub>3</sub>O<sub>4</sub> Nanoparticles

In recent decades, a variety of fabrication methods of different controllable sizes of Fe<sub>3</sub>O<sub>4</sub> magnetic particles have been developed. These methods can be generally classified into two types, which are solid-phase synthesis and liquid-phase synthesis. For liquid-phase synthesis, the liquid precursor will go through precipitation, dehydration and crystallization to obtain the product of Fe<sub>3</sub>O<sub>4</sub>, while for the solid-phase synthesis, only solid materials are involved without dissolving in any solution.

#### 1.3.1 Solvothermal Method

Solvothermal method is one of the most well-known methods for inorganic nanomaterials fabrication. This synthesis method uses solvents as the reaction medium in a reactor that can provide high pressure when operated in a high temperature (200°C to 300°C) oven. Since the

reactor is fully sealed and isolated, the reaction can happen without problems that comes from solution boiling. In this situation, insoluble materials under normal atmosphere and room temperature will tend to dissolve in the solution since their solubility will increase significantly. The morphology, size, physical and chemical properties of the nanoparticle product can be controlled by tuning the temperature and the volume of solution.

Many research groups have developed solvothermal method to fabricate  $\text{Fe}_3\text{O}_4$  nanoparticles of different structures. Sun et al.[31] uses  $\text{Fe}(\text{acac})_3$  as the iron source to synthesize the  $\text{Fe}_3\text{O}_4$  crystal seed of 4nm, and later the nanoparticles grow into bigger size of 6, 8, 12, 16nm. Other researchers reported an alternative to use  $\text{FeCl}_3 \cdot \text{H}_2\text{O}$  instead of the more expensive  $\text{Fe}(\text{acac})_3$  as the iron source[32]. Another report by Gao[33] uses  $\text{FeCl}_3$  and carbamide as precursors and alginate as the reducing agent and successfully fabricated  $\text{Fe}_3\text{O}_4$  nanoparticles of 25nm under  $180^\circ\text{C}$  for 24h. For particles that are synthesized in inorganic solution are reported to be lack of size uniformity and monodispersity while organic solvents are proven to be more helpful in controlling nanoparticle size and morphology[34, 35]. Pinna[36] used Benzyl alcohol as solvent and Iron(III) 2,4-pentanedionate to synthesize  $\text{Fe}_3\text{O}_4$  nanoparticle of different diameter with good monodispersity and uniformity in size.

### ***1.3.2 Precipitation Method***

Precipitation method is widely applied in synthesis of nanomaterials due to the simple procedure, low cost and suitable for large scale production. The most popular one of precipitation methods is co-precipitation, which is simply adding precipitant into solution that contains various types of cations until the concentration of cations are much higher than the equilibrium and therefore all components are simultaneously precipitated in proportion. For  $\text{Fe}_3\text{O}_4$ , the major reaction is[37]:



For precipitation methods, the molar ratio of  $\text{Fe}^{3+}$  and  $\text{Fe}^{2+}$  will determine the crystal structure of product while pH, concentration of the ions and reaction temperature will affect the diameter of the nanoparticles. Therefore, the major tasks for researches on this synthesis procedure will be answering how to control the crystal structure and particle sizes by adjusting different parameters in the reaction and the filtration of the leftover precipitants. Kim et al.[38] studied and reported when the concentration  $\text{Fe}^{2+}$  is lower than 1M, the product contains considerable amount of  $\text{Fe}_2\text{O}_3$  instead of purely  $\text{Fe}_3\text{O}_4$ . With the increase of the amount of  $\text{Fe}^{2+}$ , both the purity of  $\text{Fe}_3\text{O}_4$  and its saturation magnetization will be improved.

### ***1.3.3 Microemulsion Method***

Microemulsion method involves the process of two incompatible solvent forming emulsion under the presence of surfactants, which is, in other words, the continuum being separated into tiny spaces to form a microreactor where the reaction will happen and result in the solid product. Due to the restraints from microreactor in the processes of nucleation, crystal growth and agglomeration, the nanoparticles product will be covered with a surfactant layer that effectively prevents the aggregation of the nanoparticles. Based on different disperse phase and continuous phase, microemulsion method can be divided into two types, which is water-in-oil(W/O) or oil-in-water(O/W). For  $\text{Fe}_3\text{O}_4$  nanoparticles synthesis, W/O microemulsion is more commonly used.[39]

### ***1.3.4 Sol-gel Method***

For sol-gel method,  $\text{Fe}^{3+}$  are mixed with  $\text{Fe}^{2+}$  with the molar ratio of 1 to 2. Organic acid is added to regulate the pH and later a gel will be formed after slowly evaporating the solvent. With the

removal of the leftover organic materials under high temperature, the final product is obtained. Sol-gel method is chosen for its low temperature operation and product uniformity in particle size. However, this method faces challenges from controlling preparation conditions and long processing time.

### ***1.3.5 Thermal Decomposition Method***

Most cases of the thermal decomposition method use iron oxalate as the iron source. With heating process carried under high temperature, the materials will be decomposed into  $\text{Fe}_3\text{O}_4$ . For large-scale production, the advantage of this solid-phase synthesis method is obvious. On the other hand, the products fabricated via decomposition lack purity and has a wide distribution in terms of particle sizes. In the same time, a lot of energy is necessary and the amount of heat wasted in the process is significant as well.[40]

## **1.4 Application of Magnetic Nanoparticles**

$\text{Fe}_3\text{O}_4$  MNPs are widely applied in many areas owing to their unique magnetic properties. Recent years have witnessed a rapid growth of researches on  $\text{Fe}_3\text{O}_4$  in magnetic fluids, biomedicine, catalysts, contaminant removal, electronics and other fields.

### ***1.4.1 Contamination Treatment***

Iron as a strong reducing agent, is widely used in various organic and inorganic pollutants treatments in contaminated water source, especially chlorinated solvents. Due to the high surface-to-volume ratio of nanoparticles,  $\text{Fe}_3\text{O}_4$  MNPs has a relatively high adsorption capacity, which is favored for contamination treatment in many studies. Wanna et al.[41] reported an example of heavy metal removal by applying hybrid magnetic nanomaterial of

superparamagnetic Fe<sub>3</sub>O<sub>4</sub> particles and poly(methyl methacrylate). With external magnetic field, it has been demonstrated that Pb(II), Co(II), Cu(II), Hg(II) can be captured and therefore removed. In another study[42], the mechanism of adsorption is investigated to be mainly electrostatic attraction while particle surface area, pH and temperature in the solution will significantly affect the adsorption capacity of the nanoparticles.

#### ***1.4.2 Biomedicine***

Magnetic Fe<sub>3</sub>O<sub>4</sub> nanoparticles are expansively applied in biomedical related areas for its good biocompatibility and non-toxicity for cells. With its stable magnetic property, strong ability of targeting and drug carrying, as well as controllable drug releasing rate, Fe<sub>3</sub>O<sub>4</sub> nanoparticles can work as drug carrier for targeting treatment. With navigation from the external magnetic field, Fe<sub>3</sub>O<sub>4</sub> nanoparticle along with absorbed drug will travel directly to the desired lesion location. Once the nanoparticles reach the destination, drug release can be completed by heat triggering. Since these nanoparticles are superparamagnetic and do not exhibit any magnetization without external field[43], the Fe<sub>3</sub>O<sub>4</sub> nanoparticles will not be aggregated and avoid potential damage to the cells[43]. This method is proven to be efficient without much harmful side effects, which could be a potential treatment for cancer[44, 45].

Besides Drug delivery proposed as treatment for cancer, there is another type of method using Fe<sub>3</sub>O<sub>4</sub> nanoparticles that could be alternative. When applying an oscillating magnetic field of high frequency, it can lead to energy releasing in the form of heat, which then increases the temperature in the cell to an abnormal value of 41°-45°C. The damage of high temperature to cells is reversible for normal cells but irreversible for cancer cells[46]. Comparing to the traditional hyperthermia which can only apply to the whole body or close to skin tissue, the

advantage of using magnetic particles is that it can theoretically reach tumor in any places and be heated locally. The energy loss in the hysteresis cycle provides the heat for the surrounding environment. This treatment method is known as magnetic hyperthermia.

### ***1.4.3 Other Applications***

With respect to the great potentials of magnetic  $\text{Fe}_3\text{O}_4$  nanoparticles, they can be used in various applications. Among different forms and phases that the nanoparticles are presented, most of the studies focus on magnetic fluid, which is composed of a stable colloidal system with strong MNPs dispersed in the liquid. It combined the magnetic property of solid and rheological property of liquid, which is attractive for further development into applications[47]. Magnetic fluid has been applied and reached commercial maturation in the fields of dynamic sealing, speaker, computer hard drive, lubricant, vacuum equipment and so on back in 1970s [48-50]. In loudspeakers, for example, the colloidal ferromagnetic nanoparticles provide the viscous damping force on the voice coil in response to electrical excitation and therefore improve its acoustical performance[50]. In other cases such as dynamic sealing[51], the magnetorheology property of the fluid is utilized under external magnetic field. More recent applications have also been developed including photonic crystals. With its self-assembly photonic structure under magnetic field, Yin et al. has developed  $\text{Fe}_3\text{O}_4$  MNPs into color-tunable display system[52]. It has great potential for applications in many industrial areas.

## **1.5 Scope of Thesis**

This thesis focused on the application of magnetic  $\text{Fe}_3\text{O}_4$  nanoparticles in both colloids and hydrogels. For the first part, we fabricated the  $\text{Fe}_3\text{O}_4$  nanoparticles and coated with  $\text{SiO}_2$ . We utilized its self-assemble ability into amorphous crystal structure under electrical field for further development as a colorimetric voltage monitoring device, which is also demonstrated with a zinc-air battery for application. For the second part, we reviewed the three strategies of dispersing MNPs in hydrogels and discussed the traditional fields where hydrogel system with  $\text{Fe}_3\text{O}_4$  nanoparticles are applied to including drug delivery, enzyme immobilization, cell and protein separation, as well as microorganisms and organics detection and purification of wastewater. Furthermore, the operation principles and application of magnetic hydrogels in the upcoming field of soft robotics are demonstrated with examples.

Chapter 2 is the background reveals basic mechanisms of colloidal MNPs self-assembly into amorphous photonic crystal under electric field, focusing on MNPs behaviour under electrophoresis and definition of amorphous photonic crystal. This information prepared us into building a colorimetric voltmeter device later in the next chapter.

Chapter 3 of this thesis covers the synthesis procedures, experimental results, discussions and the demonstrated colorimetric voltmeter device application of  $\text{Fe}_3\text{O}_4@\text{SiO}_2$  nanoparticles in colloids.

In Chapter 4, I reviewed MNPs dispersed in hydrogels system starting from the three dispersing strategies and followed with three traditional application fields. Finally, the rapid growing field of magnetic hydrogels as soft actuators was reviewed and discussed with emphasis.

The overall conclusions of the thesis are summarized in Chapter 5.

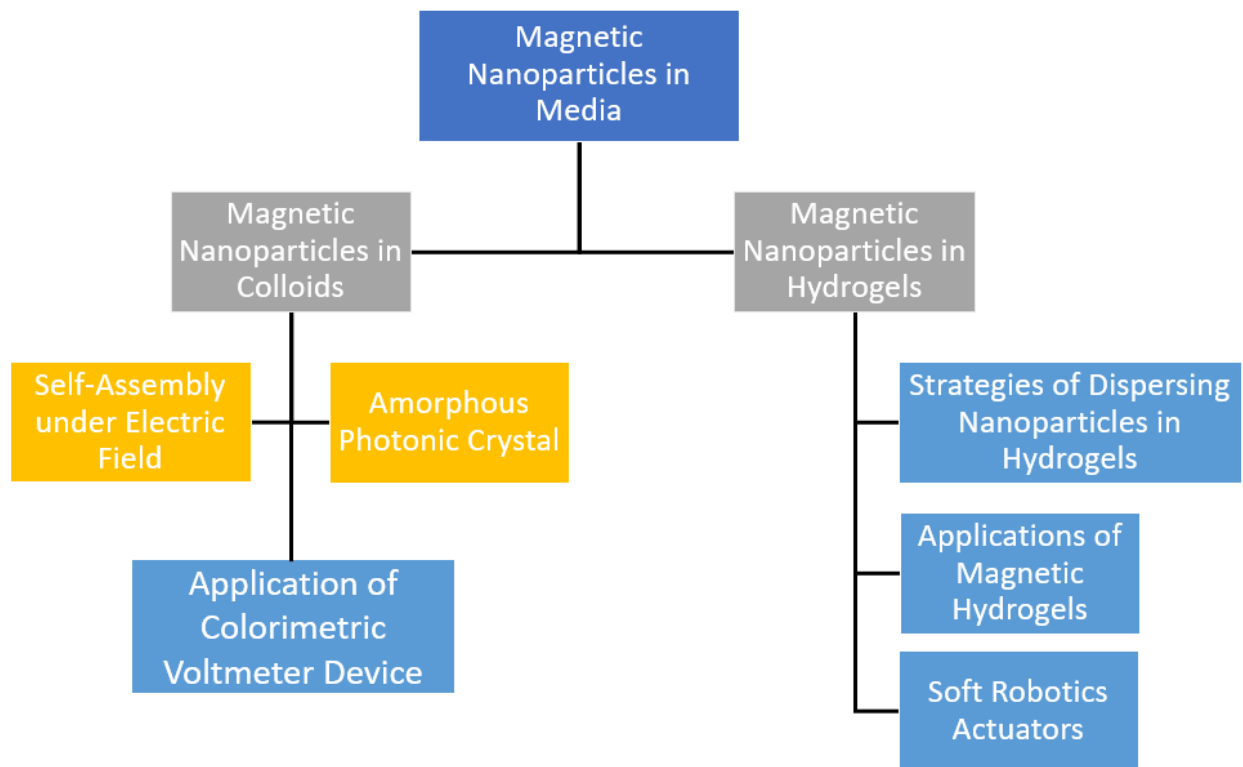


Figure 4. A summary diagram of the topics that are covered in this thesis. For the topic of colloidal MNPs, I developed a colorimetric voltmeter device by utilizing the electric field-modulated self-assembly of amorphous photonic crystal structure. For the topic of magnetic hydrogels, I reviewed the strategies of dispersing nanoparticles into hydrogel, followed by their applications with an emphasis on the emerging area of soft robotics.

## Chapter 2. Background

### 2.1 Magnetic Nanoparticles under Electric Field

#### *2.1.1 Dispersing Nanoparticles in Colloidal Suspension*

Magnetic fluids containing nanoparticles have been widely applied in various fields as we discussed in the introduction. However, large surface-to-volume ratio and surface energy of the nanoparticles renders a tendency of agglomeration between the nanoparticles. Thus, strategies to either control or avoid this problem have been important in the field[53].

For particles with zero charge, it is kinetically and energetically favorable for collision and aggregation to happen, shown in Figure 5[53]. Independent nanoparticles will combine into small clusters and larger clusters will be formed by combining the small ones. They will be settled by gravitational forces, which in the macroscopic viewpoint, is sedimentation. In order to reduce the aggregation, electrical charges on the particle surfaces will be helpful since there will be electrostatic repulsive forces involved. The repulsion between the neighbouring particles contributes to separating the nanoparticles so that they can be well-dispersed in the solution, demonstrated by Figure 5b. Based on this phenomenon, an encapsulation of nanoparticles by an inert layer of SiO<sub>2</sub> in alkaline solution has been developed as an effective method for stabilizing nanoparticles. With low isoelectric point of SiO<sub>2</sub>, the nanoparticles will not aggregation due to the electrostatic repulsion of high negative charges on the surface[54]. Ions of positive charge are drawn to the surface of the particles, while those with negative charges will be repelled away from the particle surface[55]. It will leads to the formation of electrical double layer as shown in Figure 5c[53]. Researchers have developed a wide range of models to describe it and one od the

most accepted one is from Stern[56] and Graham[57]. In this model, the counter-ion charges are located next to the particle surfaces, which is the Stern layer. Above that, there is the *Diffuse Double Layer* that contains the remnant charges distributing more broadly. For interaction, the potential ( $\psi_\delta$ ) on the slipping plane between the stern layer and the diffuse layer is more significant than the actual potential ( $\psi_0$ ) on the particle surface. Zeta potential ( $\xi$ ) is measured as the potential difference between the slipping plane and the dispersion medium. The higher the zeta potential is, the stronger the repulsion between adjacent particles will be (Figure 5d). Therefore, it will result in higher stability of the whole system.

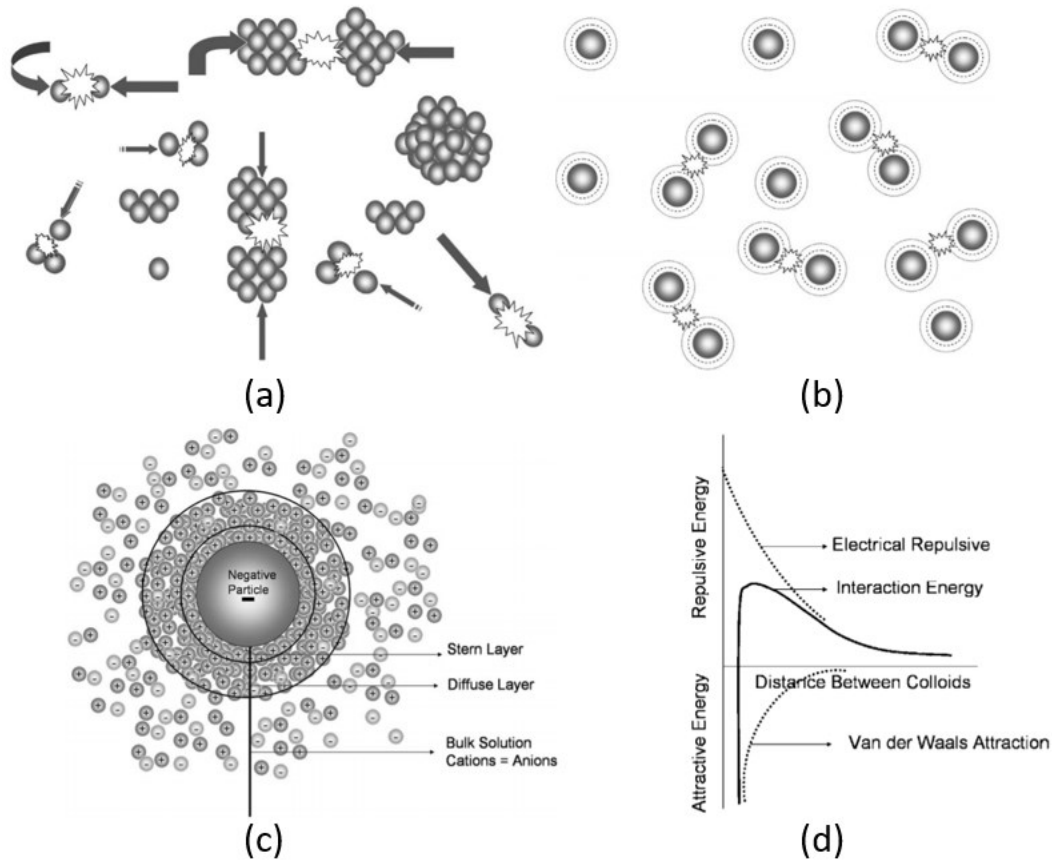


Figure 5. (a) Schematic illustration that displays uncharged nanoparticles' tendency to collide and coalescence in the favor of energy. (b) Nanoparticles can be stabilized in an aqueous

medium when they have surface charge. The ions in the double layers can protect the nanoparticles from aggregation. (c) Schematic illustrating the Diffuse Double Layer structure. (d) The dependence of the net interaction energy on the particle distance, which is the combination of repulsive and attractive energy. Reproduced with permission from [53].

### ***2.1.2 Nanoparticle under Electrophoresis***

With an external electric field ( $E$ ) applied upon the suspension, the charged particle as well as the ions in the double layer will respond at the same time. The charged particles tend to move towards oppositely charged electrode while the counterions in the double layer tends to move in the other direction. Therefore, the deformation of double layer occurs and the previous overall balance of perfect shielding of the particle collapses, and it becomes the driving mechanism of particle motion. It is also known as double layer polarization. To be exact, the polarization is only referred to the outer diffuse layer instead of the stern layer since the counterions are strongly attracted to the particle surface and they will keep sticking with the particle even in motion. The border between Stern layer and diffuse layer can be viewed as a solid-liquid interface during particle movement. Hence the velocity of particles movement is determined by the zeta potential[57].

Electrophoresis happens under the influence of a spatially uniform electric field, when dispersed particles steadily translate relatively to the fluid[58, 59]. The motion of particles under electrophoresis has been first proposed by Smoluchowski[60]. He described a rigid spherical particle with electric double layer moving in a boundless field when exposed to electrical potential gradient. The mobility of the particle can be described by the following Henry equation[61]:

$$\mu = \frac{2 \varepsilon_0 \varepsilon_r \xi}{3 \eta} f(\kappa r)$$

Where  $\varepsilon_0$  is the dielectric constant of vacuum and  $\varepsilon_r$  is the relative dielectric constant of the medium,  $\eta$  is the solvent viscosity and  $f(\kappa r)$  is the Henry coefficient, whereas  $\kappa$  is the reciprocal of the Debye length and  $r$  is the particle radius. This formula is only valid for weakly charged particles with thin double layer thickness[60].

Based on the Henry equation, zeta potential measurement is established as a characterization method. During the measurement, an electrical field is applied on the sample and the electrophoretic mobility of the nanoparticles is measured by laser Doppler velocimetry.[62]

Regarding the Henry equation, remaining terms in the equation, dielectric constant and viscosity of the solvent must be measured prior to the measurements. The result of zeta potential is highly dependent on both the surface charges of nanoparticles and the pH value of the solvent.

Generally speaking, nanoparticles with a zeta potential smaller than 10mV or larger than -10mV can be viewed as neutral. Nanoparticles with a zeta potential larger than 30mV are considered strongly cationic and those with less than -30mV are regarded as strongly anionic.[62] Both strongly cationic and anionic particles usually have a high stability and dispersion in the solution due to the strong electrostatic repulsion between the particles.

### ***2.1.3 Self-Assembly of Nanoparticles under Electrophoresis***

Induced by the uniform electric field, the charged particles in a dilute solution will experience the electrophoretic movement due to Coulombic force and become condensed near the electrode with opposite charge. With high density of the colloidal particles, they will start forming closely-packed lattice structure located close to the surface of electrode[63]. The balance of

electrokinetic force and the interparticle repulsive force is the underlying regulation of this structure thus it can be compressed or relaxed by tuning the electric field intensity.

When there is no external field applied, the colloidal particles are at rest. They will disperse in the solution randomly and there is no structure forming. Under electric field of certain intensity, the balance will be collapsed, which results in electrophoresis. Charged particles will be stacking near the oppositely charged surface with lattice structure. As the field intensity increasing, the electrophoretic will become higher and the interparticle repulsive forces should be matched with it. In this case, it will lead to the closer distance between charged particles so that repulsion between them will be much stronger. Eventually, the overall structure formed will be compressed to be denser. On the other hand, when the field intensity is decreasing, the structure will be relaxed due to the forces balancing and canceling with each other. By doing this, we can easily control the magnitude of the structure by changing the field intensity.

However, for the particles that are away from the electrode surface, they will also experience the repulsive forces from the layers that are closer to the electrode, in addition to the forces mentioned above. As described in the Figure 6[63], layers of charged particles that are far from the electrode have an increasing larger interparticle distance since the accumulated repulsion from the previous layers are higher. Based on this, we can see that the particle arrangements are dependent on the distance between particle and the electrode, so that the overall formed structure of particles under constant electric field has only short-ranged order, which can be also tuned by simply altering the field intensity.

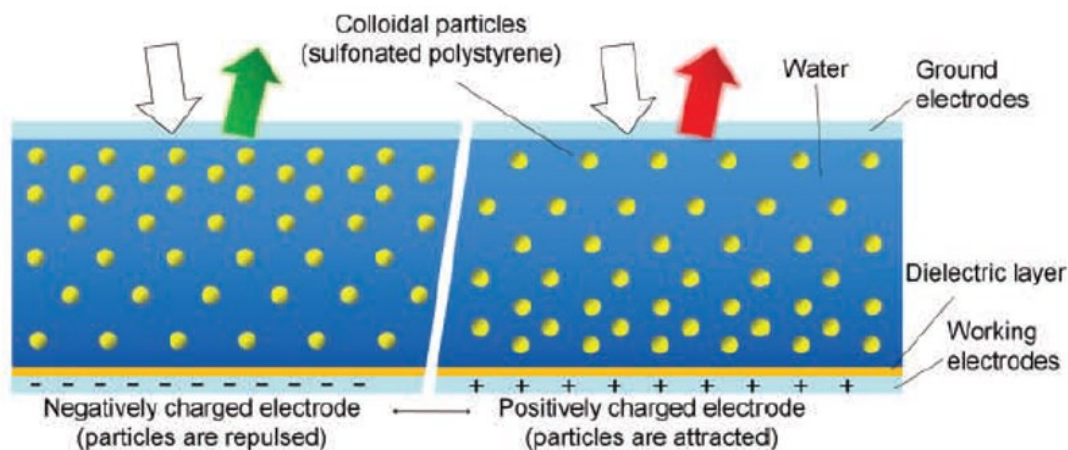


Figure 6. Schematic illustration of the self-assembly of colloidal nanoparticles under electrical field. Reproduced with permission from [63].

## 2.2 Amorphous Photonic Crystal

### 2.2.1 Structural Colour

Structural colour is a form of physical coloration that comes from the interaction of incident light and the micro/nano structures of the materials itself, including reflection, interference and diffraction.[64, 65] Comparing to the traditional chemical colour (pigmentation), structural color is attracting an increasing attention as a result of being more environmentally friendly and energy saving. In nature, structural colors are widely observed, such as butterfly wings, chameleon skin and parrot feathers[66, 67]. The first ever scientific description of structural color can be dated back to 1665, when British scientist Robert Hooke recorded his observation of feathers of birds in the book of *Micrographia*. He found that the waterdrop will affect and destroy the color of feathers and assumed that the alternating of air and water films increased the inverted color to the light and therefore reduced the light intensity. Another milestone in understanding structural color was the Maxwell's development of electromagnetic theory in 1873 and the experimental

research on electromagnetic wave by Hertz in 1884, which later lead to two different opinions in the field, namely, surface color and structure color[68]. In 1895, Walter proposed that iridescent color in nature is a result of surface reflection with pigments, and the change in color with incident light is caused by absorbing the reflection polarization of the edge, which is also supported by the experimental results of Michelson[69]. Later in 1917, Lord Rayleigh used the electromagnetic theory and derived an equation of the reflection property of regular layered medium. He pointed out that some colors of insects and butterflies come from the crystal structure of skin and feathers, therefore the exhibited color is greatly dependent on the incident light unlike the pigmentation. He denied “surface color” and insisted that multilayer diffraction is the real cause of structural color[70]. Followed by many other researches by Onslow[71], Merritt[72], Mason[73], thin film interference theory was developed and became the mainstream doctrine to explain structural color with experimental findings under the microscope.

Recent decades have witnessed the further developments in the field of structural color. Based on the physical interaction of incident light and micro/nano structure, the mechanism of structural color can be classified into five categories: thin film interference, multilayer interference, diffraction grating, light scattering and photonic bandgap[74].

Thin film interference is most common cause for structural color in nature. Due to the difference of refraction index of the mediums, the incident light will be reflected at both upper and lower interfaces of the thin film and the reflected light will also interfere with each other. As a result, thin film interference will either enhance or reduce the reflected light with certain wavelength based on the thin film thickness. Multilayer interference shares the same mechanism with thin film interference except that the incident light is reflected much more times at different interfaces and the reflected light will experience a phase shift at each boundary. For diffraction grating

effect, when parallel incident light enters a multi-silt structure, diffraction will happen at every silt and diffraction strips will be formed consequently. When the silts are ordered in one direction, each strip will be perfectly overlapping at certain distance and the total intensity distribution is an interference superposition of independent stripes[75]. Light scattering, proposed first by physicist Raman in 1928, describes the propagation of the uniform incident light in a medium that contains materials with different refractive index can lead to a non-uniformity in light propagation[76]. These impurity materials are usually particles, and they disperse irregularly in the medium. In this case, incoherent scattering will happen, and the reflected light can be viewed at different angles.

When two materials of different dielectric constants arrange periodically, photonic bandgap will be formed. In this structure, light wave with certain energy will be prohibited to enter. By adjusting the size of units in the periodic structure, it can be used for filtering light waves with different frequency ranges. Photonic bandgap structure has been widely applied in filters, amplifiers, and other optical communication devices. Based on the long-range periodicity of the micro/nano structural units, photonic bandgap materials can be categorized into three types, which are photonic crystal (PC), amorphous photonic crystal (APC), and random structure.[77] Among them, both PC and APC as the most representative photonic bandgap materials have received tremendous attention in recent decades.

### ***2.2.2 Photonic Crystal***

Photonic crystal is a long-range ordered structure with special translational symmetry. When light enter this type of periodic structure, a band structure with photonic bandgap will be formed due to Bragg's diffraction. Photon with energy in the range of photonic bandgap will be reflected

selectively instead of travelling inside the structure. If the wavelength of reflected light falls into visible light range, the structure will exhibit certain color, which is the ordered structural color.

Ever since John[78] and Yablonovitch[79] proposed the concept of photonic crystal back in 1987, it has been studied and developed thoroughly. Based on their research, photonic crystal is defined as materials of different dielectric constants periodically stacking into micro/nano optical structure. The intrinsic characteristic of photonic crystal is the photonic bandgap in the band structure. The spatial distribution dimension of the photonic bandgap determines the dimensions of the scattered light. With the respect to dimensions, photonic crystal can be categorized into three type[80]: 1-D, 2-D and 3-D photonic crystals. These structures show materials stacking in one, two and three directions respectively so that we can control the dimensions of photon band for the incident light.

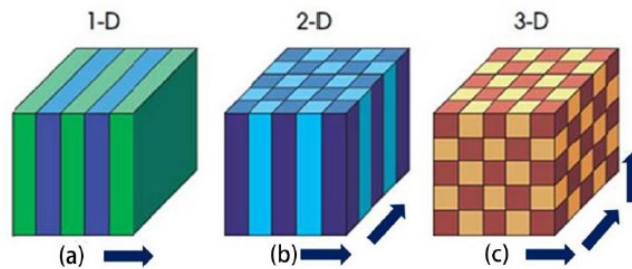


Figure 7. Examples of 1-D, 2-D, 3-D photonic crystals. Different colors represents materials with different dielectric constants. Reproduced with permission from [80].

Methods of fabricating photonic crystal have investigated, which includes Top-Down, Down-Top methods and template. One of the most popular method among them is the self-assembly method, which is one type of Down-Top method. In general, the prepared and dispersed particles

(components) in a solution can be spontaneously assemble through non-covalent interaction into a specific ordered nanostructure. These non-covalent effects include hydrogen bonding, van der Waals forces, electrostatic forces, hydrophilic and hydrophobic interactions, gravity, applied magnetic or electric fields, capillary forces, and so forth. Some researchers divided these methods into two categories according to the energy change in the assembly system, which are static and dynamic.[81] For static self-assembly, the process takes place in a balanced environment. Once the ordered structure is formed, it will remain stable without consuming more energy. On the other hand, dynamic self-assembly occurs in an unbalanced environment. It requires continuously energy supply, and the resulting structure is remains in a dynamic changing status. Comparing these two types of methods, dynamic assembly is preferable for practical applications including sensors and actuators and attracts more attention in the field. Commonly used dynamic self-assembly mainly includes magnetic field self-assembly and electric field self-assembly.

Magnetic field induced self-assembly photonic crystal structure was first proposed by J. Bibette in 1993.[82] When exposed to external magnetic field, monodispersed  $\text{Fe}_2\text{O}_3$  emulsion will form a highly ordered structure and its color can be tuned to yellow, green, red or blue. The experiment result show that this color change can only be observed at the direction of magnetic field instead of any other viewing angle. The exhibited color changed with both the external field and the diameter of the emulsion droplet. There was not enough clue for further explanation for the phenomenon. Later in 2001, Asher *et al.*[83] presented a work of  $\text{Fe}_3\text{O}_4@PS$  nanoparticles with highly charged surface assembling into periodic photonic crystal structure under magnetic field. The reflection light of this structure experienced a blue shift with increasing magnetic field intensity, and it realized the multicolor band with single particle size photonic crystal. To further

improve the uniformity of the nanoparticles and address the interference of electrostatic repulsion from the charges to the magnetic forces due to low magnetic permeability, researchers have been focused on developing different material system and fabrication methods. One of the research teams, Yin and his colleagues[14] used solvo-thermal method to synthesize MNPs and successfully assemble them into colloidal 1D chain-like photonic crystal in the direction of magnetic field. Their color results show high reflectivity and better optical properties.

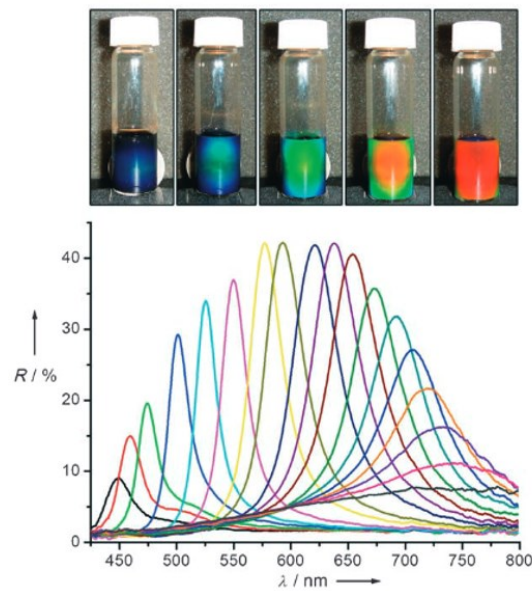


Figure 8. Colors of colloidal 1-D chain-like photonic crystal tuned by the external magnetic field and the reflectance spectrum results with peaks ranging from 450nm to 750nm. Reproduced with permission from [14].

### ***2.2.3 Amorphous Photonic Crystal***

Amorphous photonic crystal has a different structure than photonic crystal for there is no long-ranged order but only short-ranged order of stacking. Amorphous photonic crystal can be widely

found in nature, shown in Figure 9.[77] While some bird feathers are made of photonic crystals that exhibit iridescent colors viewing from different positions, some bird feathers have amorphous structure that shows non-iridescent color and remains same color from varying angles. For example, the red macaw's feather barb shows a non-iridescent blue due to its amorphous diamond photonic crystal structure.[84] Random close-packed and spin-decomposed structures were also found on the scales of some long-horned beetles, which showed a bright, non-iridescent color. For many decades, many researchers hypothesised this blue color is an result of incoherent scatterings from the air cavities[85], such as Rayleigh or Mie scattering. However, Raman suggested that the cavities are not small compared to the wavelength of light. And instead, he believed that interference from the surfaces of films are the reason of the formation of blue color.[86] Later in 1970s, Dyck proposed a different hypothesis that coherent scattering of light with certain wavelength by the fine air cavities are the cause of the angle-independent color. [87] After 20 years, Dyck applied the electromagnetic theory of coherent light scattering and proved the color observed color is from the constructive interference of light through spatially distributed scattering.[88]

Since the color of amorphous photonic crystal is stable and not varying with viewing angle, it meets the requirements of designing most applications such as colorimetric sensing, display system and other optical devices. For these reasons, researches in this structure inspired by nature findings received an increasing attention in recent decades[89].

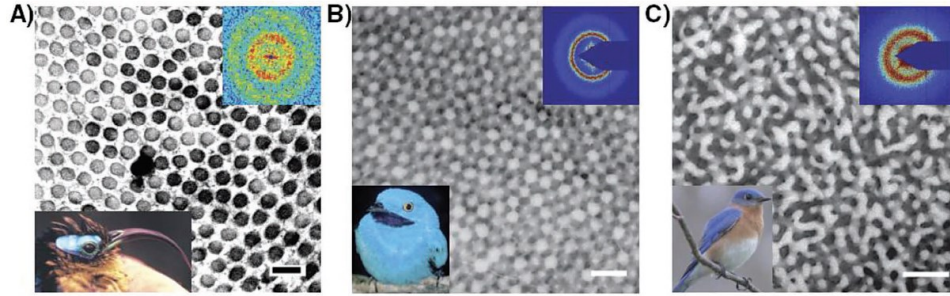


Figure 9. SEM photos of amorphous crystal structures in different birds' feathers. Reproduced with permission from [77].

Amorphous photonic crystal can be viewed as a defective structure of photonic crystal with low order of lattice arrangement. These defects have a random distribution in the structure which breaks the long-range order. In order to study this random close-packing model(RCP) theoretically, Dong *et al.*[90] used a finite-difference time-domain(FDTD) spectral method[91] run a simulation on the model RCP photonic structures generated by rate-dependent densification algorithm[92]. The RCP photonic structure was built as a cubic supercell of  $(14.9d)^3$  ( $d$  is the particle diameter) which contains 4000 nanoparticles spheres. They calculated the photon density of states (PDOS) of the RCP structure as a function of reduced frequency  $d/\lambda$ , shown in Figure 10, where  $\lambda$  is the wavelength in vacuum. The PDOS of a system demonstrates the number of photonic states available at each frequency. As shown in the result, two notable dips appear in the PDOS. However, unlike the photonic gaps in conventional photonic crystal structure, which show zero in the PDOS, the photonic pseudogaps here in amorphous structure have nonzero PDOS. In addition, as a consequence of the random distribution and non-orientation of the units in amorphous crystal, the photonic pseudogap is therefore isotropic and light will be scatter equally in all directions. In another study, optical properties of a Si-rod-connected APC with an amorphous-diamond symmetry were studied using similar method[93]. Besides the pseudogaps,

the existence of a photonic bandgap (PBG) with zero PDOS is revealed upon increasing the refractive index contrast. The transition from pseudogap to PBG confirmed that the long-range order is not a necessary factor for PBGs to form.

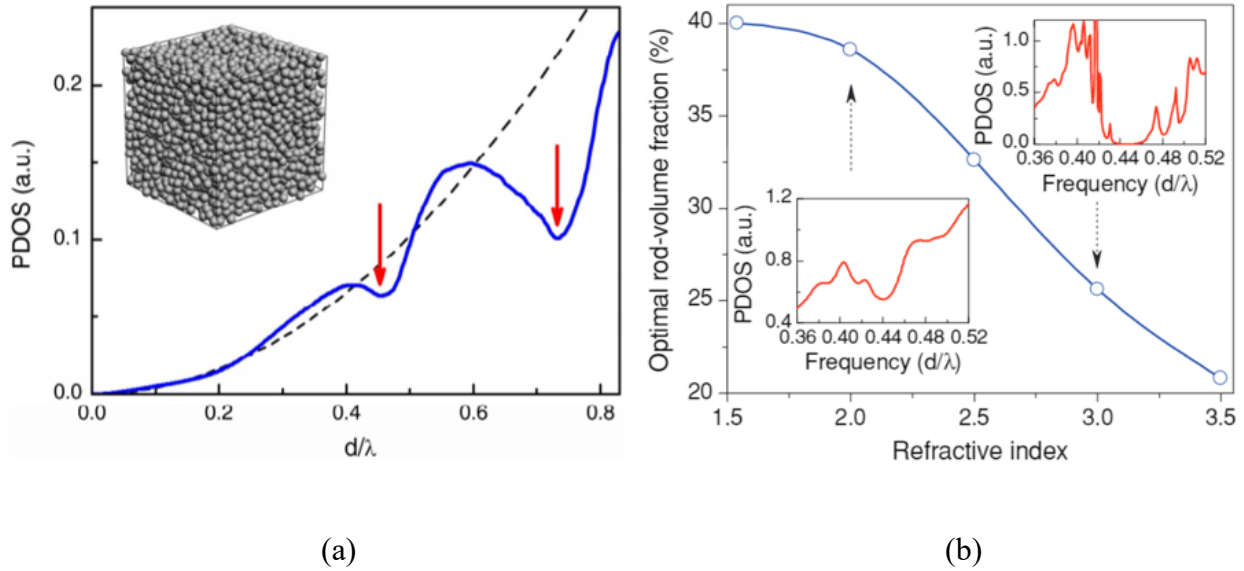


Figure 10. (a) PDOS of the RCP structure as a function of reduced frequency  $d/\lambda$ . Two dips are shown where pseudogaps are located. Reproduced with permission from [90]. (b) The transition from pseudogap to PBG with increasing the refractive index contrast of the materials.

Reproduced with permission from [93].

There are generally three types of fabrication methods for building amorphous photonic crystal structure: colloidal self-assembly, template, and phase separation. Being the most popular method of these three, self-assembly in amorphous photonic crystal synthesis shares the same general procedures with the one previously discussed for traditional photonic crystal. J.D. Forster

used the solution containing two different polymeric nanoparticles and spin-coating it onto a glass surface.[94] In their approach, they mixed the PS nanoparticles of 226nm and 271nm in the emulsion and fabricated a blue thin film. With evidence of SEM photos, it is clear that the particles are stacking in an approximately random order. Therefore, the color from the thin film is non-iridescent. Another approach from Takeoka[65] used two monodispersed SiO<sub>2</sub> particles with different diameters and self-assembled them into amorphous structure to obtain the angle-independent structural color material. Furthermore, the color can be tuned by adding different ratios of two particles. Regarding to controlling the self-assemble process more precisely, Lee *et al.*[95] applied an external electric field to control the Fe<sub>3</sub>O<sub>4</sub>@SiO<sub>2</sub> MNPs movement. The amorphous photonic crystal structure with angle-independent and fast-response structural color is formed and it can achieve full-color display by tuning the field intensity.

## **Chapter 3. Colorimetric Voltmeter Using Colloidal**

### **Fe<sub>3</sub>O<sub>4</sub>@SiO<sub>2</sub> Nanoparticles as an Overpotential Alarm**

#### **System for Zinc-air Battery**

### **3.1 Introduction**

Photonic crystals (PCs), wherein microstructure regulates the diffraction of light to produce a specific colour, draw increasing attention as a platform for colorimetric sensing.[96, 97]

Conventional PCs exhibit long-ranged structural periodicity, which leads to multiple Bragg scatterings that results in a photonic band gap (PBG). Consequently, the display of colour of the conventional PCs is iridescent, which means that the colour varies with respect to the viewing angle.[98] Such unique property has been utilized in many applications from photonics to optoelectronics.[14, 99, 100] Recently, amorphous photonic crystals (APCs), wherein the microstructure has some degree of short-range order but lacks long-range periodicity, receive special attention.[77] Unlike conventional PCs, APCs display non-iridescence as the result of coherent light scattering of its isotropic structure.[101, 102] In case of colloidal assembly of nanoparticles (NPs), APCs are when the interparticle distance matches the length scale of the wavelength of visible light, whereas the tuning the interparticle distance modulates its colour.[95] The absence of iridescence renders APCs to have merits over PCs in applications such as displays and colorimetric sensors.

For sensor and display applications, APCs require an ability to modulate colour with respect to external stimuli.[103] A colloidal solution of Fe<sub>3</sub>O<sub>4</sub> NPs with electrostatically charged surface

are shown to be the one of suitable candidates owing to their tunable self-assembly to balance magnetic dipole attraction with electrostatic repulsion.[13] However, the high surface energy ( $>100$  dyn/cm) of  $\text{Fe}_3\text{O}_4$  NPs requires unrealistic amount of specific surface area and magnetization to prevent aggregation between NPs in water and organic solvents.[104, 105] To address this problem,  $\text{Fe}_3\text{O}_4$  core covered with amorphous  $\text{SiO}_2$  shell ( $\text{Fe}_3\text{O}_4@\text{SiO}_2$ ) has been suggested, whereas  $\text{SiO}_2$  shell provides a facile solution for controlling the NP size, achieving surface uniformity, and stabilizing the dispersion in the colloid. In alkaline solutions, the surface of the  $\text{SiO}_2$  shell is negatively charged.[95] Based on the balance of electrophoretic movement and the electrostatic repulsion between the nanoparticles, a tunable APC structure can be formed under variable electrical field.

For the formation of  $\text{SiO}_2$  shell, Stöber method, in which silica is formed through alkaline hydrolysis of tetraethyl orthosilicate (TEOS) in ethanol/water mixture, is commonly used.[106] Before the shell formation, the  $\text{Fe}_3\text{O}_4$  core requires a stabilization step in ethanol/water mixture to prevent their aggregation in the precursor solution.[107] Various surfactants were used in the stabilization of the  $\text{Fe}_3\text{O}_4$  core.[108-110] Among the surfactants, trisodium citrate were proven to enhance dispersion by introducing the electrostatic repulsion between the NPs due to di-carboxyl groups that provide negative charges in alkaline solution.[105, 111]

Electrically responsive PCs have shown promises for full-color electrophoretic display applications.[112] For such application, PCs are required to have high electrophoretic mobility, NP size monodispersity, and high optical contrast and low voltage response.[113] Various NPs, including a random copolymer of poly(methylmethacrylate-*co*-styrene) [114],  $\text{TiO}_2$ -coated silica[115], and  $\text{TiO}_2$ [116], were conducted for this application. However, there are still remaining challenges to overcome such as limited visibility and controllability of the reflected

colour.  $\text{Fe}_3\text{O}_4@\text{SiO}_2$  was chosen to overcome these hurdles since it has high optical contrast ( $\text{Fe}_3\text{O}_4$  has the refractive index of 2.42) and controllable sizes.[95, 117] Compared to neat  $\text{SiO}_2$  NPs, the incorporation of  $\text{Fe}_3\text{O}_4$  core is shown to be effective in enhancing the electrophoretic mobility and colloidal stability of the core@shell NPs.<sup>10</sup> Such merits in electrophoretic displays are directly relevant to colorimetric sensor applications.

In the pursuit of developing novel solid-state batteries in academic setup, aging of batteries, often due to catalyst failures, is one of the most outspoken challenges.[118-120] An intuitively perceivable real-time monitoring system for such battery failure can be greatly helpful. There has been numerous alarming methods available in market since last century, but they usually require complicated electrical circuits.[121, 122] A simple alternative is by using LED indicators, but these LED enable digital mode operation (i.e. binary on/off status) whether the battery output is above or below a pre-set threshold voltage.[123] For continual monitoring of battery output degradation, however, an analogue operation (i.e., continuous colorimetric modulation) may be more effective in certain applications. Here, we propose that electrically responsive APCs can provide a real-time battery performance monitoring system at a minimal parasitic energy consumption.

In this chapter, we report a colloidal APC with electrically tunable and non-iridescent color display as an aging indicator for solid-state zinc-air battery. Here,  $\text{Fe}_3\text{O}_4@\text{SiO}_2$  NPs were dispersed in polycarbonate solution, whereas  $\text{Fe}_3\text{O}_4$  cores were solvothermally synthesized and then their surfaces were modified by citrate, followed by  $\text{SiO}_2$  shell coated by Stöber method to achieve a stable colloidal APC. We then fabricated a voltage colorimetric device where the NP solution was injected into the gap between two indium tin oxide (ITO) plates, and then connected to a solid zin-air battery. As a result, we could monitor the real-time voltage output information

of the zinc-air battery, including discharging, charging, overcharging and aging-induced degradation, by analyzing the color display of our APC. In this way, we demonstrated the tunable optical property of APC can find a promising application in monitoring battery performance in real-time.

## **3.2 Materials**

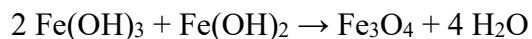
Sodium citrate ( $\text{Na}_3\text{Cit}$ , dihydrate) and 95% denatured ethyl alcohol was purchased from Fisher Scientific. Sodium acetate (anhydrous,  $\geq 99\%$ ), ethylene glycol (anhydrous, 99.8%), propylene carbonate (anhydrous, 99.7%), ammonium hydroxide solution (28.0%-30.0%  $\text{NH}_3$  basis), tetraethyl orthosilicate (99.999% trace metals basis) were purchased from Sigma Aldrich and were used without further purification. Iron (III) chloride hexahydrate ( $\text{FeCl}_3 \cdot 6\text{H}_2\text{O}$ , bulk, 97%) was also purchased from Sigma and was grinded into powder only prior to experiments to prevent hydrolysis in the air.

Indium tin oxide coated glass slide (8-12  $\Omega$  /sq) was purchased from Sigma Aldrich and used for device fabrication. Polyvinyl alcohol (PVA) (molecular weight: 146,000~186,000), Zinc sheet, potassium hydroxide ( $\geq 85\%$  KOH basis), platinum, ruthenium, carbon paper and copper sheet were purchased from Sigma Aldrich to fabrication the solid-state zinc-air battery with polyelectrolyte.

## **3.3 Methods**

### ***3.3.1 Experimental Methods***

*Fe<sub>3</sub>O<sub>4</sub>@SiO<sub>2</sub> Nanoparticles Synthesis.* Fe<sub>3</sub>O<sub>4</sub> was synthesized based on solvothermal method. 0.318g of sodium citrate was first dissolved in 20ml of ethylene glycol and mixed thorough in the sonicator. This solution A was then heated at 50°C with constant magnetic stirring for 20min. The solution B containing 0.819g of FeCl<sub>3</sub>·6H<sub>2</sub>O dissolved in 10ml ethylene glycol was then transferred and mixed with solution A. After that, 1.5g of sodium acetate was introduced into the solution, followed by 1.5ml of DI water. The mixture was then transferred into an autoclave and heated in the oven for 10h at 200°C. The chemical reaction of the formation of Fe<sub>3</sub>O<sub>4</sub> are proposed as below:



*SiO<sub>2</sub> coating process was conducted based on the Stöber method.*[106] After purifying the nanoparticles with ethanol and DI water sequentially, a quarter of the product (50mg) was dissolved in 6ml DI water and 40 ml ethanol. 2ml of 14% ammonium hydroxide solution was introduced into the mixture and then transferred into a flask. At 90°C water bath, 200µl of TEOS was added into the mixture slowly (100 µl each time at a 20 min interval) with stirring at 600rpm for 40min. The product is collected afterwards and washed with ethanol and DI water for three times each. The schematics of the synthesis is shown in Figure 11a.

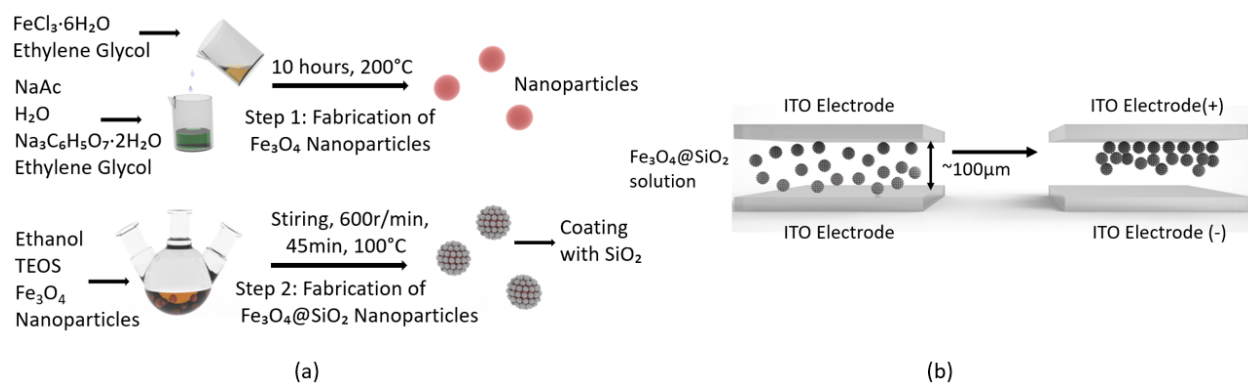


Figure 11. (a) A schematics of synthesis procedure of  $\text{Fe}_3\text{O}_4@\text{SiO}_2$  nanoparticles. (b) Schematic illustration of the working mechanism of our colloidal amorphous photonic crystals (APCs) as a battery performance indicator.

*Battery Performance Indicator Device Fabrication.* The  $\text{Fe}_3\text{O}_4@\text{SiO}_2$  NPs was dried overnight in the oven at  $60^\circ\text{C}$ . Then the product was dissolved into propylene carbonate with the weight ratio of 0.15:0.85 and mixed well in bath sonicator for 2h to create a colloidal APC solution.

Two ITO-coated glass slides were cleaned with acetone, DI water and ethanol in a sequence. After drying, two strips of double-sided tape were placed between two slides to create a gap of  $100\ \mu\text{m}$ . The colloidal APC solution was then injected into the gap. With respect to the applied voltage between the glass slides, the color of the device was modulated. The schematics of the device under operation is shown in Figure 11b.

*Zinc-Air Battery Fabrication.* Zinc-air batteries are generally composed of three parts; pure zinc metal as the anode, an air electrode as the cathode, which is divided into a gas diffusion layer (GDL) and a catalytic active layer, and a layer of polyelectrolyte as the separator, as shown in Figure 12a[124]. Oxygen from the atmosphere diffuses into the porous carbon electrode under

the difference of pressures of oxygen between the outside and inside of the battery cell, and then the catalyst facilitates the reduction of oxygen to hydroxyl ions in the alkaline electrolyte with electrons generated from the oxidation of zinc metal as the anode reaction. Generated hydroxyl ions migrate from the air cathode to the zinc anode to complete the cell reaction. Both oxygen evolution reaction (OER) during the charging process and the oxygen reduction reaction (ORR) during the discharging process will take place at the air cathode.

In order to facilitate these two reactions, two highly active and robust oxygen electrocatalysts were selected, which are platinum(Pt) for ORR[125] and ruthenium(Ru) for OER[125, 126] . Porous carbon paper is chosen as the material for the gas diffusion layer(GDL) since it allows air to permeate. PVA-KOH gel was chosen as a popular solid electrolyte since it is proven to provide enhanced conductivity and desirable mechanical robustness as a result of the low crystallinity and high degree of water retention.[127]

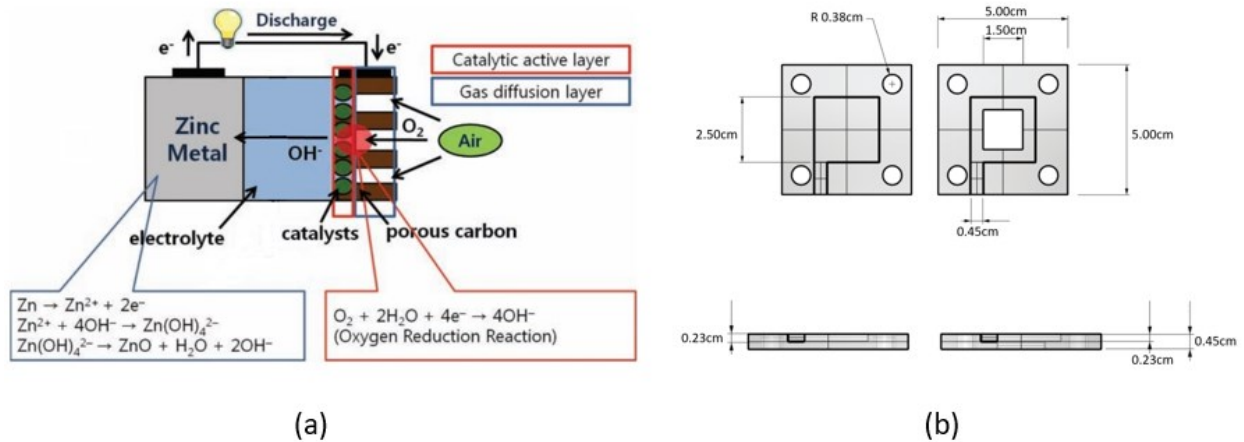


Figure 12. (a) Zinc-Air battery working principle and reactions on each electrodes. Reproduced with permission from [124]. (b) Battery Encapsulation Acrylic Mold Specification.

*Air Cathode Preparation.* Pt/Ru catalyst ink was prepared and sprayed onto the GDL substrate. The ink consisted of 50 mg of Pt/Ru/C powder (40% Pt and 20% Ru, Alfa Aesar), dispersed in 2.0 mL of DI water, 0.1 mL of 5 wt% Nafion (D-521), 1.0 mL of isopropanol and 0.2 mL of 10 wt% polytetrafluoroethylene (PTFE) (DISP30). The mass loading of Pt/Ru/C ink on the GDL substrate was around  $0.6 \text{ mg cm}^{-2}$  after drying in a furnace at  $300^\circ\text{C}$  for 30 min.

*PVA-KOH Electrolyte Preparation.* The high molecular weight PVA (molecular weight: 146,000~186,000) was dissolved in the distilled water (10%) at  $80^\circ\text{C}$  and mixed for 3h. The sample was then exposed to low temperature at  $-20^\circ\text{C}$  overnight and then three more cycles of thawing for 2 h at  $25^\circ\text{C}$  and freezing for 2h at  $-20^\circ\text{C}$  to let them crosslink. After the freeze-thawing process, the sample was cut into small piece ( $L=0.1 \text{ cm}$ ,  $S=0.9 \text{ cm}^2$ ) and immersed into 30 mL KOH solution of 6M at room temperature overnight.

*Battery and Monitoring Device Assembly.* A piece of zinc metal sheet, PVA-KOH gel and carbon paper with catalysts were assembled layer by layer and fully encapsulated vertically in the acrylic mold made by laser-cutting, which specifications are shown in Figure 12b. Two copper strips were used as the connectors to link the ITO glass slides of the indicator device to the two electrodes of battery respectively. In this way, the indicator device was parallel to the battery in the circuit for real-time measurement of the voltage. With encapsulation of this mold, polyelectrolyte can have a longer life span and each components of the battery as well as the connectors can be in full contact with each other to ensure the battery performance being sensed by the monitoring device.

### ***3.3.2 Characterization Methods***

Both Fe<sub>3</sub>O<sub>4</sub> nanoparticles and Fe<sub>3</sub>O<sub>4</sub>@SiO<sub>2</sub> nanoparticles were characterized and compared with scanning electron microscopy (Zeiss Sigma (Gemie) Field Emission - Scanning Electron Microscope (FE-SEM) images and x-ray diffraction (Rigaku Ultima IV XRD) results. Dynamic Light Scattering and Zeta Potential were conducted for both nanoparticles by using Zeta-sizer (Zetasizer Nano S90, Malvern Panalytical). The colorimetric response of the colloidal APC indicator device was monitored under a regulated DC current (E3630A, Agilent) is directly visible and its quantification was done by image processing from a digital camera (A6000, SONY). Charge-Discharge test and rate test was done using a potentiostat (PGSTAT302N, Autolab, Metrohm).

## **3.4 Results and Discussion**

### ***3.4.1 Material Characterization***

SEM images of the fabricated Fe<sub>3</sub>O<sub>4</sub> and Fe<sub>3</sub>O<sub>4</sub>@SiO<sub>2</sub> NPs are shown in Figure 13a. For Fe<sub>3</sub>O<sub>4</sub> NPs, it is visible that the surface is very rough with bulges of nanocrystals that aggregated. For Fe<sub>3</sub>O<sub>4</sub>@SiO<sub>2</sub> NPs, on the other hand, the surface is significantly smoother. The average particle size is increased with SiO<sub>2</sub> shell layer, as also can be confirmed by dynamic light scattering (Fig 13b). The average diameter of the Fe<sub>3</sub>O<sub>4</sub> NPs is measured to be 79.2nm with a broad size distribution, whereas Fe<sub>3</sub>O<sub>4</sub>@SiO<sub>2</sub> NPs show a significantly narrower size distribution with an increased average diameter of 91.2nm. The PDI (polydispersity index) value for Fe<sub>3</sub>O<sub>4</sub> and Fe<sub>3</sub>O<sub>4</sub>@SiO<sub>2</sub> are 0.203 and 0.174 respectively. The zeta potential of Fe<sub>3</sub>O<sub>4</sub> and Fe<sub>3</sub>O<sub>4</sub>@SiO<sub>2</sub> (Fig

13c) are measured to be -40.4mV and -56.1mV respectively. Zeta potential ( $\xi$ ) is measured as the potential difference between the slipping plane in the Diffuse Double Layer Model and the dispersion medium.[57] The higher the zeta potential is, the stronger the repulsion between adjacent particles will be, which therefore results in higher stability of the whole system. Generally, a specific value of zeta potential higher than 30mV or lower than -30mV can be recognized as an electrostatically stabilized system.[128] These results support our hypothesis that including SiO<sub>2</sub> shell brings surface charges that leads to dispersion stability in the colloidal system.

From the XRD pattern of Fe<sub>3</sub>O<sub>4</sub> NPs in Figure 2d, the peaks at  $2\theta$  values of 30.1°, 35.5°, 43.1°, 57.0°, 62.6° are indexed as the diffractions of [2 2 0], [3 1 1], [4 0 0], [4 2 2], [5 1 1], [4 4 0] planes, respectively, of the cubic spinel Fe<sub>3</sub>O<sub>4</sub> (JCPDS PDF#88-0866). The reflection angles and relative intensities of the XRD peaks of our Fe<sub>3</sub>O<sub>4</sub>@SiO<sub>2</sub> NPs are mostly identical to that of Fe<sub>3</sub>O<sub>4</sub>[129]. Comparison between the peaks from Fe<sub>3</sub>O<sub>4</sub> and Fe<sub>3</sub>O<sub>4</sub>@SiO<sub>2</sub> assures that there is no additional peak since the SiO<sub>2</sub> shell formed by Stöber method is amorphous.

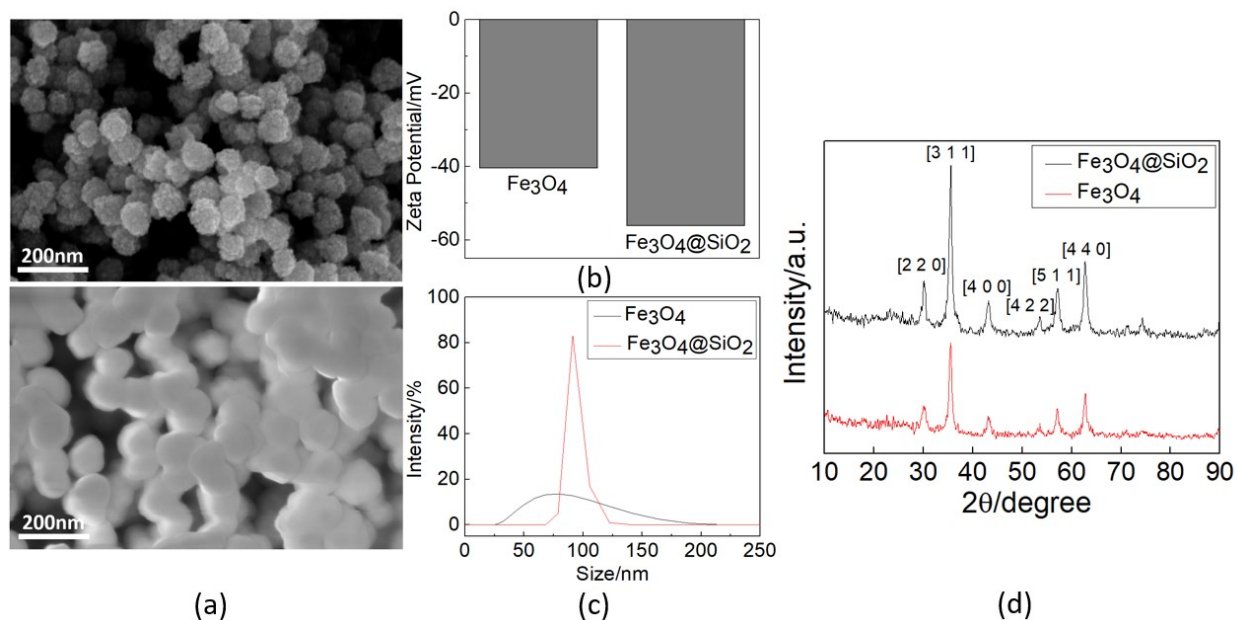
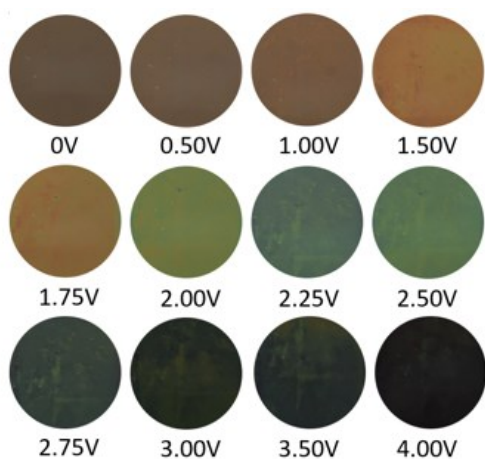


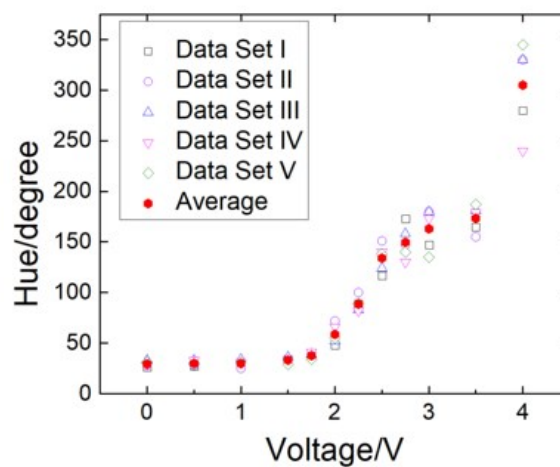
Figure 13. (a) SEM image of  $\text{Fe}_3\text{O}_4$  (above) and  $\text{Fe}_3\text{O}_4@\text{SiO}_2$  nanoparticles (below).

Comparisons of (b) zeta-potential, (c) Dynamic light scattering results, and (d) XRD patterns of  $\text{Fe}_3\text{O}_4$  and  $\text{Fe}_3\text{O}_4@\text{SiO}_2$ .

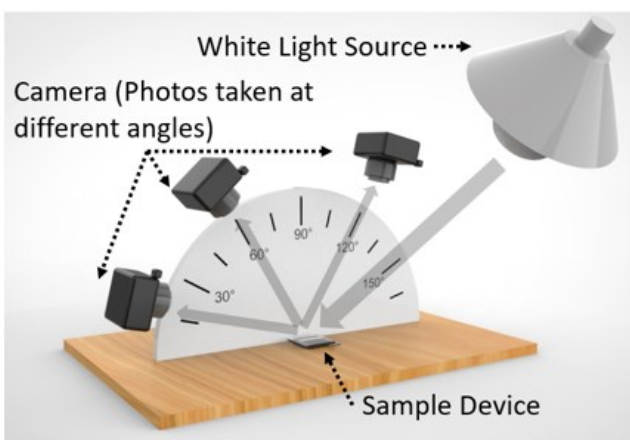
### 3.4.2 Voltmeter Device Application



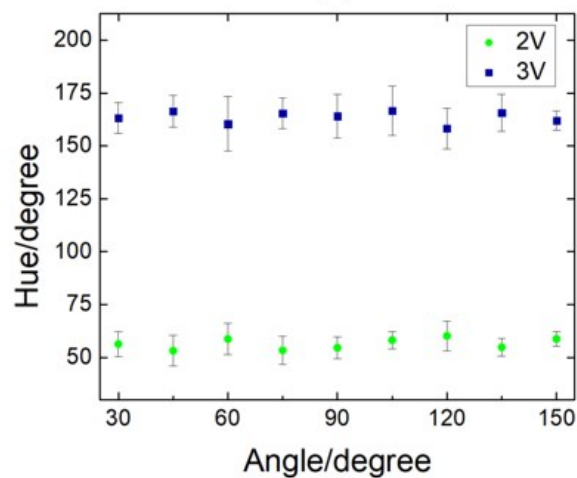
(a)



(b)



(c)



(d)

Figure 14. (a) Colorimetric displays of the colloidal APC device under various voltages. (b) Hue-Voltage calibration curve of nanoparticle device. (c) Schematic Illustration of the angle-dependence measurement. (d) Angle dependence on hue of the nanoparticle device's colour display.

Figure 14a shows digital camera images of the colloidal APC device displaying ranges of colour under applied voltages. The applied electric field varied from 0 to 400 V/cm with the interval of 25 V/cm. Colour changes are distinguishable to naked eyes. Quantitative analysis of the colorimetric response can be done by extracting color parameters from the digital images. The most well-known color parameter is RGB (red-green-blue) function, where a given colour is described as mixture of the three primary colours of light. However, in case of colloidal APC device, where the wavelength of the light is modulated over a large range, hue-saturation-value (HSV) color function is preferred because the color information is stored in a single parameter of the hue.[130-133] The lighting conditions may affect the saturation and value but not hue. This makes hue in HSV color function a reliable parameter for quantitative characterization the colorimetric response of the device.

We connected our device to a DC power source and recorded the colorimetric response of the colloidal APC device under applied voltages between 0 and 4 V. Hue values were extracted from five sets of images using MATLAB and plotted verse voltages (Figure 14b). The average values are plotted with red solid dots. The colorimetric response times of our device to voltage change are typically within 50ms and 170 ms for on-switching and off-switching respectively, in accordance with a previous report.[95] Under operating conditions of the colloidal APC device,

the NPs form a short-range ordered structure in the solvent as a result of balancing the magnetic dipole attraction, electrostatic repulsion between charged surfaces, and the externally applied electric field. The movement of the charged NPs under electrophoretic force will lead to a formation of densified structure near the interface on the positive electrode. For particles that are relatively far from the interface, the force that they sense is much lower due to shielding from the opposite charges of the NPs at the electrode interface and therefore the structure built is less compact with increasing distance to the positive electrode[63]. Therefore, an amorphous photonic crystal structure with only short-ranged color is formed and the photonic color displayed is angle-independent. When applied electric field increases, the average distance between the NPs becomes shorter, leading to a blue-shift in the colorimetric response, as our results shows a transition from red to green (*i.e.*, an increase in hue value) as applied voltage increases.

In order to characterize the property of amorphous photonic crystals, we carried a hue-angle dependence measurement outlined in the schematics in Figure 3c. We took digital photos of the sample device operating under 2V and 3V respectively at different viewing angle ranging from 30° to 150°. After extracting the hue parameter using the same method as mentioned above and plot the data points with viewing angle (Figure 3d), we found out that the hue parameter remained steady with changing angles, at hue= 57°(±7°) and 163°(±12°) respectively, which proved that the color is stable and independent from viewing directions. The angle-independent color is unique for amorphous photonic crystal structures and it provides reliable information for the device applications.

Here, one may wonder how an amorphous structure without long-range order displays specific colour in a deterministic manner with respect to applied external voltage. The structural color of

crystalline PC comes from the existence of PBG. APC can be viewed as a PC with an extreme content of defects. A computation model of random close-packing model (RCP) with a finite-difference time-domain (FDTD) spectral method shed light to understand the origin of colour in APC[134]. A photon density of states (PDOS) calculation of APC by Dong *et al.* has shown two notable dips appear in the PDOS at certain frequency, which is then referred as pseudogaps[90]. Unlike the PBGs in PC structure that show zero PDOS, the photonic pseudogaps in APC have nonzero PDOS. In addition, the photonic pseudogap lacks directionality as a consequence of the amorphous nature. When there is a stark contrast in refractive index in APC, the pseudogap may even have zero PDOS, which can be considered as PBG[93]. In other words, crystallinity with a long-range order is not a necessary factor for PBGs to form.

It is noticeable that the colorimetric response of the colloidal APC device shift from red (1.0V) to orange (1.5V), to green (2.0V) and then to dark olive green (2.5V). The potential range falls perfectly into the normal operational conditions a zinc-air battery[135, 136]. Eventually, the device will turn nearly into black at 4V, at which the average hue is 305°. The colour shift is fully reversible.

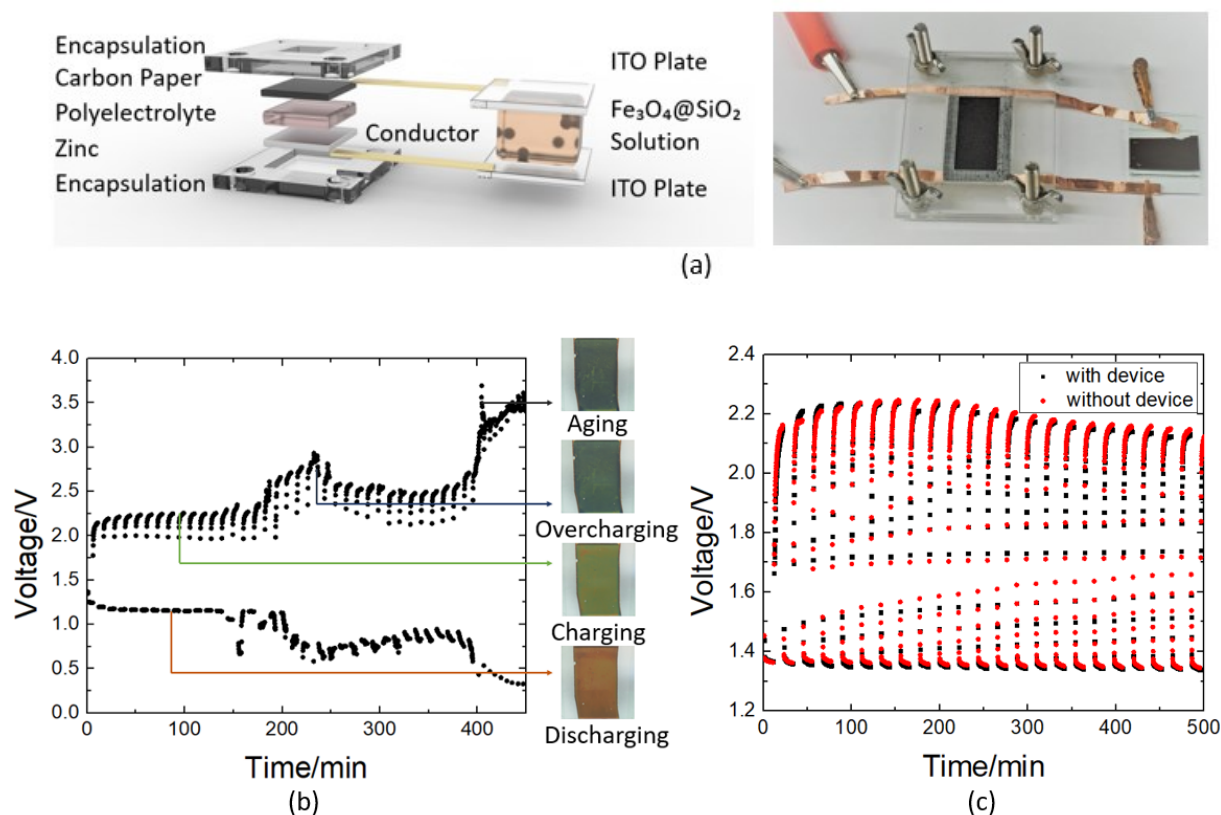


Figure 15. (a) (left) Schematic illustration of battery and the APC device configurations and (right) the image of the actual battery and device. (b) Charge-discharge curves with overcharging, aging situations with colorimetric indication by the colloidal APC device. (c) Charge-discharge curves for battery without (red) and with (black) the colloidal APC device attached.

A custom-made jig to evaluate the performance of zinc-air battery with our colloidal APC device was fabricated (Figure 15a). Using the setup, cycling tests of the battery were conducted through a galvanostatic method with 12 min per cycle by the potentiostat. The zinc-air battery was charged and discharged at  $5 \text{ mA cm}^{-2}$  for 5 minutes each cycle and the circuit was kept open for 1 min between steps. A total of 40 cycles was done on the battery. In order to create a scenario of overcharging,  $20 \text{ mA cm}^{-2}$  was used in some cycles, as shown in Figure 15b. Overcharging

happens when there is not enough  $\text{Zn(OH)}_4^{2-}$  to consume when charging, usually induced by charging for an over long time or extra higher current.

A real-time operation example shown in Figure 15b exhibits four different stage that a zinc-air battery may undergo: discharging, charging, overcharging and aging (towards eventual death). Before aging, the APC device displays orange (Hue:  $30.1^\circ$ ) and light green (Hue:  $85.3^\circ$ ) during discharging and charging conditions, respectively. Under abnormal operations, the APC device will alarm users by showing dark blue (Hue:  $149.6^\circ$ ) to warn about overcharging. When the device is nearing its death, the APC device will show black colour (Hue:  $246^\circ$ ) to indicate extreme overcharging. In short, our colloidal APC device can effectively indicate the condition of zinc-air battery.

In order to test whether there is any adverse effect to zinc-air battery performance, we also examined the influence of attaching the colloidal APC device. The cyclic tests were set up as 8 min each for charging and discharging at  $5 \text{ mA cm}^{-2}$  per cycle, with the interval of 2 min between steps and a total of 30 cycles was performed. Since the device is simply made of two small ITO plates and a dielectric colloid in between, it can be viewed as a small capacitor with measured capacitance of  $\sim 350 \text{ pF}$ , which is not likely to cause any parasitic power consumption under DC operation condition. In other words, our colorimetric voltmeter will not add a significant “burden” to the battery. As shown in Figure 15c, essentially identical charge-discharge curves of zinc-air battery with and without attached device supports this argument.

### 3.5 Conclusion

In summary, we have demonstrated a colorimetric voltmeter as an overpotential alarming device for zinc-air battery using the self-assembled  $\text{Fe}_3\text{O}_4@\text{SiO}_2$  nanoparticles induced by electrical field. With the coating shell layer of  $\text{SiO}_2$ , the MNPs disperse and stabilize better in polycarbonate solution due to the repulsion forces. Under voltage from 1.0V to 2.5V, which is also the working voltage range for zinc-air battery, the nanoparticle device showed discernible color changes from red to dark blue. We also proved that our nanoparticle device system is composed of amorphous photonic crystal, which exhibits angle-independent colors by the hue-angle dependence measurement. When attached to a working battery, the device indicates four battery behaviour with a simple connection by copper tape, including discharging, charging, overcharging and aging. Without difficult and equipment-based electrical measurements, this device shows considerable potential application in battery behaviour monitoring.

## Chapter 4. Recent Progress in Magnetic Hydrogels

### 4.1 Strategies to Disperse Magnetic Nanoparticles in Hydrogels

Magnetic hydrogel is an inorganic and organic composite. Its dimension can be modulated by external magnetic field. Typically, it is composed of the polymer network and magnetic nanomaterials. Common magnetic materials including iron ( $\text{Fe}_3\text{O}_4$ ,  $\gamma\text{-Fe}_2\text{O}_3$ ), cobalt, nickel, manganese and their alloys, oxides, permanent magnet materials (rare earth minerals) are used widely, among which  $\text{Fe}_3\text{O}_4$  magnetic powder or magnetic fluid are the most popular choices for magnetic hydrogels.[137, 138] Polymer networks for hydrogels can be divided into three categories, which are synthetic hydrogels, semi-synthetic hydrogels and natural hydrogels. Natural polymers are extracted from natural sources including plants, humans and animals. They can be further classified based on the composition into proteins (such as collagen, gelatin, silk, etc.), polysaccharides (such as alginates, agarose, chitosan, etc.) [139]. Synthetic polymers are produced by human deriving from the petroleum oil, such as poly(glycolic acid) (PGA), poly(lactic acid) (PLA) and their co-polymers poly(lactide-co-glycolide), polycaprolactone (PCL), poly(propylene fumarate), polyethylene glycol (PEG) and polyurethane. Semi-synthetic hydrogels are blended by synthetic artificial polymers and natural polysaccharides.

Magnetic hydrogels are attracting increasingly attention in the many academic fields due to its unique properties in biocompatibility, biodegradability and magnetic responsiveness, etc. These properties are greatly dependent on the hydrogel materials, size of the MNPs, and their distribution in the hydrogel networks, as well as preparation conditions. Based on the

combination of the nanoparticles and the hydrogel networks, the synthesis methods of magnetic hydrogels can be categorized into three types: blending, in situ precipitation and grafting-onto methods, as shown in Figure 16.[138]

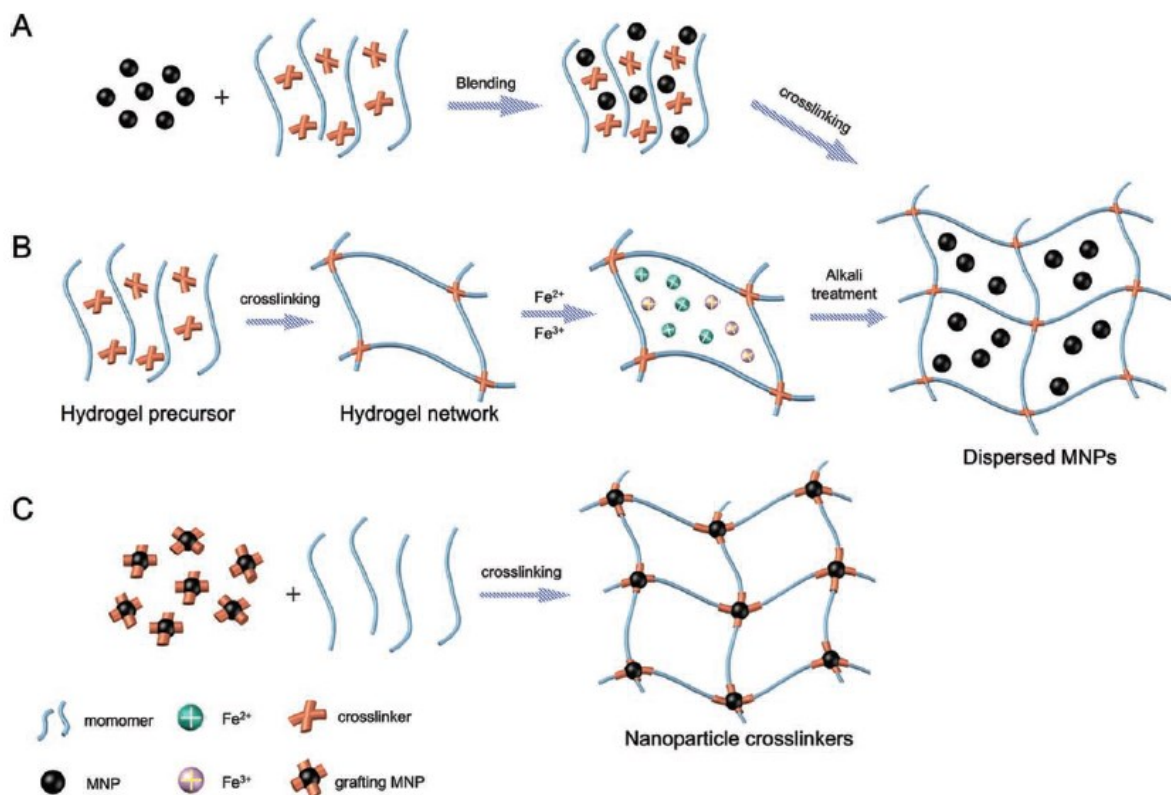


Figure 16. Strategies to disperse MNPs in hydrogels: (a) blending method; (b) in-situ precipitation method; (c) grafting-onto method. Reproduced with permission from [138].

#### 4.1.1 Blending Method

Blending Method, also known as physical doping, is the process of mixing the prepared MNPs and the hydrogel monomers (or polymer precursors) solution at certain ratio. During the

crosslinking step, the MNPs will be encapsulated in the three-dimensional network structure of the hydrogels. The outline of the preparation process is described in Figure 16a. Blending method is so far the most popular method for its advantages in simple reaction conditions and easy operations since it separates the process of fabrication and encapsulation of MNPs, which also enables researchers to blend the MNPs with a wide range of particle diameters from nanometers to micrometers. However, challenges remain in controlling the distribution and dispersion of the MNPs in the hydrogel structures. In addition, the MNPs dispersed in the network are easily diffused into the solution because of the lack of strong bonding between the MNPs and the hydrogel network, which negatively affects the structural stability of the magnetic hydrogel. Tong et al.[140] in 2010 published a work on poly(N-isopropylacrylamide) (PNIPAAm)/Fe<sub>3</sub>O<sub>4</sub> magnetic hydrogels using the blending method, where they used suspension polymerization to fabricate the magnetic hollow microcapsules and core-shell hydrogel beads. In another work, Ahmad et al.[141] mixed Fe<sub>3</sub>O<sub>4</sub>/SiO<sub>2</sub> nanocomposite particles with a temperature-responsive hydrogel precursor microemulsion, and prepared the magnetic hydrogel microspheres by physical doping. The analysis of its morphological structure, size distribution and volume phase transition showed that the composite hydrogel has a core-shell structure and the magnetic particles are located at the center. It has been found that the composite hydrogel has both temperature responsiveness and magnetic responsiveness, which leads to a promising future of the material to be used in biological separation, drug carriers and other fields. Toth et al. [142] modified the surface of magnetic particles (MNPs) with biocompatible chondroitin-A (CSA) to obtain CSA-encapsulated MNPs (CSA@MNPs), which were introduced into hyaluronic acid by physical doping. Rheology studies have shown that the presence of the CSA@MNPs component

does not affect the rheology of the hydrogel. The hydrogel can be applied to biomedical preparations for intra-articular injection for the treatment of osteoarthritis.

#### ***4.1.2 In situ Precipitation Method***

The in situ precipitation method uses a pre-prepared hydrogel as a reactor, and by swelling in an aqueous solution of iron salt so that  $\text{Fe}^{2+}$  and  $\text{Fe}^{3+}$  can diffuse into the three-dimensional network structure. After adding the precipitant, the  $\text{Fe}_3\text{O}_4$  nanoparticles are formed in the hydrogel network, as shown in Fig 16b. The  $\text{Fe}_3\text{O}_4$  nanoparticles prepared by this method are uniformly dispersed and large amount of MNPs can be introduced into the matrix. On the other hand, this method is only suitable for specific hydrogels that has good stability of the hydrogels under basic condition or the network could be destroyed by alkali solution. Furthermore, due to the use of alkali solution, the application of the magnetic hydrogels prepared by this method is limited in certain biological areas such as cell encapsulation. Zhao et al.[143] blended O-acetyl-galactoglucomannan (AcGGM), crosslinker (epichlorohydrin) with  $\text{Fe}^{2+}$ ,  $\text{Fe}^{3+}$ . Under  $60^\circ\text{C}$ , reactions of crosslinking and fabrication of  $\text{Fe}_3\text{O}_4$  take place in the alkaline solution simultaneously. They successfully prepared the hemicellulose-based hydrogels (MFRHHs) with magnetic responsiveness by in-situ formation of  $\text{Fe}_3\text{O}_4$  nanoparticles. In their results, magnetic property characterization showed that the magnetic hemicellulose hydrogel has good magnetic sensitivity, and the magnetization increases in tandem with the increase of the content of the MNPs. Further observation by scanning electron microscopy revealed that MFRHHs had a uniform macroporous structure, and agglomerates of  $\text{Fe}_3\text{O}_4$  nanoparticles adhered to the pore walls.

#### ***4.1.3 Grafting-onto Method***

The grafting-onto method is also a commonly used method for preparing magnetic hydrogels. Different from the former two methods, the method crosslinks the modified MNPs as a crosslinking agent with the polymer precursor by grafting a reactive group which can further chemically react on the surface of MNPs. The preparation process thereof is shown in Figure 16c. The magnetic hydrogel prepared using this method has covalent bonds between the MNPs and the hydrogel network, which results in an excellent stability of the whole system. Jiang et al.[144] prepared an attapulgite/fly ash/polyacrylic acid (ATP/FA/PAA) ternary magnetic nanocomposite hydrogel by introducing acrylic modified stevensite nanorods (org-ATP) onto the inorganic framework as crosslinkers and strengthening agents. The grafting rate of the hydrogel obtained under different experimental conditions was tested. The results showed that 95% of the monomers in the best magnetic hydrogel had been grafted onto the inorganic material and had high mechanical stability and magnetism. The hydrogel exhibits good selective adsorption of  $Pb^{2+}$ , and the adsorbed ions can be completely desorbed with aqueous hydrochloric acid. These characteristics make the material have great potential for  $Pb^{2+}$  contamination in water treatment studies. Messing[145] and his team modified the surface of  $CoFe_2O_4$  MNPs with silicone-based unsaturated methacrylic acid, and used it as a cross-linking agent to covalently bond with polyacrylamide (PAAm) to prepare magnetic hydrogel. The research team proposed the structural model of the magnetic hydrogel based on the experimental results, in which  $CoFe_2O_4$  MNPs act as junction points in the gel network, and these MNPs are connected by a long PAAm polymer segment. The connection point structures in the hydrogel network can be clearly observed by transmission electron microscopy (TEM).

## 4.2 Traditional Applications of Magnetic Hydrogels

### 4.2.1 Drug Delivery

Due to the good swelling ratio of three-dimensional network structure, magnetic hydrogels can expand or contract in volume when stimulated by an applied magnetic field, which results in a different releasing rate and releasing amount of drug with hydrophobic or hydrophilic properties. In addition, an applied external magnetic field of certain intensity can change the fluidity of the drug-loaded hydrogel and gradually move the drug to the lesion area, so that the drug will gather at the target site. This will ensure that the drug functions only in a certain place and reduce the negative toxic side effects of the drug, while increasing the local drug concentration and therefore enhance the effects at the targeted area. Chen *et al.*[146] mixed the polyethylene glycol hydrogel and Fe<sub>3</sub>O<sub>4</sub> magnetic particles and went through a couple of freeze-drying cycles to form a smart magnetic hydrogel. When a DC electromagnetic field is present outside, the drug gathers around the hydrogel and the targeting process is completed.

There are generally two types of mechanism to control the drug releasing process. The first one is by controlling the magnetic moments under a static field with nanoparticle aggregating inside the hydrogel. In the same paper, Chen *et al.*[146] synthesized a PVA gel containing Fe<sub>3</sub>O<sub>4</sub>. In the absence of external field, the magnetic moments of the nanoparticles are non-oriented and the drug release happens slowly by normal diffusion only. With the applied static magnetic field, the particles will aggregate inside the gel and it leads to a bulk magnetic moment. At this time, the pores of the hydrogels are “close” and the drug release rate is dramatically decreased. The second method involves the magnetothermal effect of the nanoparticles. Hydrogels that are thermal sensitive being used in the system can be heated up by the MNPs exposed to a high

frequency oscillating field. The heat comes from the hysteresis of the nanoparticles. In the work by Hilt *et al.*[147], temperature-responsive hydrogels, poly (N-isopropylacrylamide), were used with Fe<sub>3</sub>O<sub>4</sub> embedded. Once exposed to the pulses of high frequency alternating magnetic field, the heat created will transfer to the hydrogels and leads to the phase transition with temperature higher than the lower critical solution temperature (LCST). The hydrogel will therefore collapse, leading to rapid drug releasing rate. The method can be further used in creating a drug reservoir with larger control range over the releasing rate. Hoare *et al.*[148] fabricated a drug reservoir based on ethylcellulose containing a great amount of drug and thermoresponsive nanogels. Outlined in Figure 17b, the drug releasing rate is relatively low with the absence of external magnetic field. When exposed to an alternating magnetic field, the thermoresponsive nanogels is heated, which leads to a phase transition of the nanogels. It further results in the volume contraction of the gels and the drug releasing rate is therefore increased significantly. This approach shine light into designing drug reservoir with controllable rate over at least 2 orders of magnitude (0.1-10 μg/h).

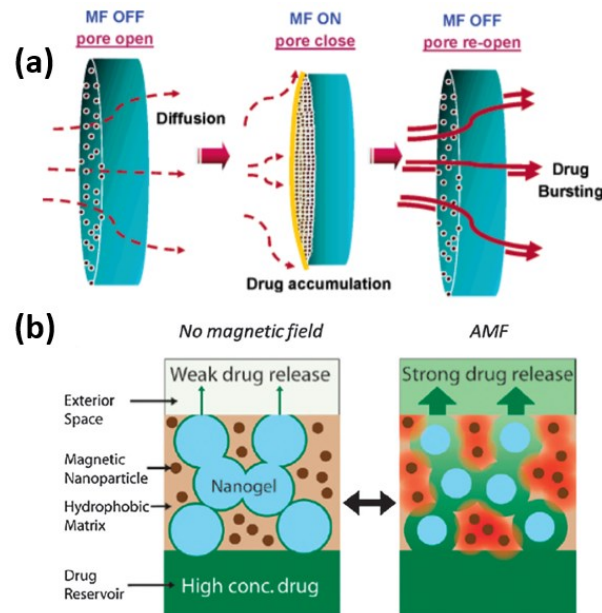


Figure 17. Controlled drug release by magnetic hydrogels. (a) Mechanism 1: Pore closure upon the presence of oscillating magnetic field Reproduced with permission from [146]. (b) Mechanism 2: Pores open with the presence of magnetic field controlled by the phase transition of hydrogels. Reproduced with permission from [148].

#### ***4.2.2 Enzyme Immobilization, Cell and Protein Separation***

Enzyme is a biological protein catalyst. With magnetic hydrogels encapsulating the enzymes, the movement of enzymes can be controlled via tuning the external field by controlling the gels. And therefore it will improve the catalytic efficiency while maintaining the activity and stability of the enzyme. Enzyme stabilization is usually realized by covalent bonding between the hydrogel network chains or MNPs and the proteins. The magnetic hydrogel system can have more than one interaction connects with enzyme. It will help to improve the thermal stability of the enzyme and restrict the protein molecule movement upon heating.[138]

After modifying biologically active adsorbents or other ligands on the surface of the magnetic hydrogel, they can be specifically combined with a specified cell or protein. Under the applied magnetic field, the hydrogel can separate, classify the cells or isolate the proteins for later analysis based on their types efficiently.

#### ***4.2.3 Detection and Purification of Microorganisms and Organics in Wastewater***

Magnetic hydrogels can significantly improve the complex and time-consuming detection methods of traditional pretreatment solution samples by applying their ability of adsorbing detected substance or harmful organic substance. In this way, target microorganisms can be

quickly separated under magnetic field with a high and stable adsorption rate. The phenomenon can be both useful in content detection of the sample solution and direct removal of microorganism or organic substance from the wastewater. Lo et al.[149] synthesized a magnetic hydrogel. By electrostatic adsorption, ions in the solution can be moved and sedimented. The water resource that contains natural organic matter will be effectively recycled and reused eventually.

#### ***4.2.4 Magnetic Induced Actuation in Magnetic Hydrogels: From Small-scale Traditional Applications to Large-scale Soft Robotics***

For the traditional three applications above mentioned, the size of magnetic hydrogels samples is relatively small (~millimetre range) [150, 151]. The actuation mechanisms cover magnetic field guiding movement, magnetothermal effect, magnetic particles aggregation and selective attractions for substances in these small-scale applications.

When applied in relatively large-scale soft robotics field, the length scale of magnetic hydrogels is substantially bigger (centimeters to meters).[152, 153] The actuation here depends on either magnetothermal effect or magnetic attraction for shape distortion, which will be discussed in the following sections.

## **4.3 Magnetic Hydrogels in Soft Robotics**

### ***4.3.1 Introduction of Magnetic Hydrogels in Soft Robotics***

Soft robotics have been a rapidly developing field in recent decades and researchers have published the great amount of works focusing on designing artificial muscles and actuators that

are sensitive to a variety of factors including thermal, light, magnetic, electric and solvent stimuli.[154] Magnetically responsive hydrogels are among promising solutions in soft robotics due to their ability for non-contact manipulation. The mechanical behaviour of the magnetic hydrogels, including elongation, coiling, torsion, rotation or bending[154] can realized by tuning the external field in many ways such as varying the field intensity, changing the field direction, introducing different field gradients or alternating the field at different frequencies. Magnetic hydrogels have combined the advantages of gel, being mechanically soft and high elasticity and the magnetic susceptibility from the particles, which enables its functionality. The fact that it can be controlled remotely from a relatively far distance provides possibility to interact with other objects, such as tissues, human skin, etc. In addition, the transition of most movement can be tuned very fast. In many researches, magnetic hydrogels showed instantaneous shape distortion upon adding or removing the magnetic field. It happens due to the superparamagnetic property of the MNPs especially for the ones that are smaller than 50 nm.[25] As we discussed previously, it will lead to zero magnetization upon the removal of the external field without nearly zero relaxation time. This will benefit to the actual robotics experiments interacting with human. When some negative events happen, the actuators can be turned off immediately. All of these advantages have made magnetic hydrogels as one of most significantly promising type of smart or intelligent materials.

#### ***4.3.2 Discussions on different types of magnetic hydrogels mechanism and the future trend***

Generally, two types of magnetic hydrogels actuators controlled by different magnetic fields stimuli are studied and their responding mechanisms are different as well. Most magnetic hydrogels are mechanically controlled by the applied magnetic fields, either homogenous or with field gradients. For others that uses the alternating magnetic field, the controlling mechanism

relays in the magnetothermal effect of the magnetic particles, which are used in shape memory hydrogels heavily. Being the first one in the magnetic hydrogel field, Zrinyi and his group [155] used the blending method to synthesize a chemically cross-linked poly(vinyl alcohol)(PVA) hydrogel filled with magnetite nanoparticles. The shape distortion of the gel was manipulated instantly by applying and removing external magnetic field. When placed in a homogenous field, there is no force putting onto the magnetic particles and thus it will not change the shape of the hydrogel. On the other hand, given a spatially non-uniform magnetic field, MNPs will sense the strong magnetic forces, which leads to the strong interaction forces between the particles and the polymer chains and lead to movement of the whole magnetic hydrogels as one unit. [138, 155] In terms of the influence of the magnetic field, using similar fabrication steps but different materials, Caykara et al.[156] reported  $\text{Fe}_3\text{O}_4$  nanoparticles dispersed in poly(N-tert-butylacrylamide-co-alkylamide) [P(NTBA-co-AAm)] hydrogel and their results show a relation between bending angle of the actuators and the applied field intensity, as showed in Fig 18a. In Zrinyi's first work, except the influence of the field, they also discussed the significant effects on the performance by varying the nanoparticle concentration (up to 8 vol.%) and the elastic modulus of the hydrogels which can be realizing by changing the crosslinking density. Higher sensitivity to the field is found related to the increase of particles concentration. However, the increase of nanoparticles amount also leads to the new crosslinks created between the chains and therefore the elasticity and the stretchability becomes worse for the system. Therefore, they attempted to improve the performance by decreasing the crosslinker amount. Similar issues were also found in other studies even in highly stretchable and tough magnetic hydrogel system of alginate-coated  $\text{Fe}_3\text{O}_4$  and PAAm, reported by Yang et al.[30]. They made a demonstration of cantilever bending beam actuator and varied the content of MNPs from 1-20 wt%. Their result

showed a maximum of compression strength of 5.6 MPa at 5 wt% doping and the mechanical performance (stretchability and toughness) continues to lower with higher content of nanoparticles, shown in Figure 18b. It remains a challenge to solve this problem of balancing the magnetic field responsiveness and the mechanical properties of the hydrogels. Another approach by Stark[157] has been proposed using different fabrication mechanism as an attempt to tackle this challenge. Here they used the Co metal nanoparticles instead of oxides for higher saturation magnetization and they also incorporated the nanoparticles as the crosslinkers into the polymer backbone. They reached a 60wt% content of the metallic cobalt in the hydrogels, which can be stretched up to 123% under magnetic field without significant mechanical property loss.

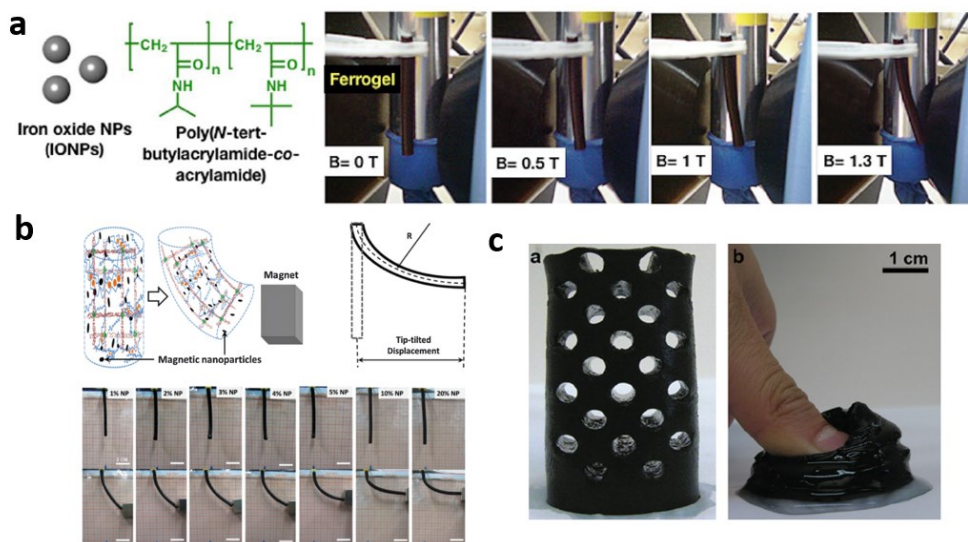


Figure 18. (a) Bending experiment of magnetic hydrogel. Reproduced with permission from [156]. (b) Bending process of magnetic hydrogel with different nanoparticles content under the magnetic field. Reproduced with permission from [30]. (c) Highly flexible metallic cobalt hydrogels under compression. Reproduced with permission from [157].

In the case of controlling alternating magnetic field to actuate the magnetic hydrogels by magnetothermal effect, shape memory behaviour of the composite is controlled by tuning the temperature to the switching temperature of the hydrogel. Lendlein group[158, 159] designed an approach to fill the temperature-memory polymer with MNPs and fabricate a shape memory actuators prototype. As illustrated in Figure 19a, a fixation device consisted of a hook with shape memory and a lock were used to demonstrate the idea. They separated the heating from the environment and the heating from the alternating magnetic field and designed different situations, where Figure 19a-iii shows the hook going into the lock under both environmental and magnetic heating and a-iv is the case when environment is the only heat source. The controlling from the magnetic field can be more precise since the temperature in the materials corresponds to a certain magnetic field intensity. In this way, the temperature-memory materials are therefore transformed into magnetic-memory materials. In another study of Vernerey et al.[160], a soft hydrogel crawler with remotely triggered motility was developed using a temperature-sensitive NiPAAm hydrogel. The hydrogel can reversibly contract when heated above the LCST and restored back to the original shape with temperature decreased. Using similar concepts as the Lendlein group, the magnetic hydrogel crawler being put a confined box can elongate and contract itself by switching the alternating magnetic field repeatedly, which then results in the movement forwards and backwards. These device samples could be further used in soft robotics or surgical applications as demonstrated by another work of Gracias et al.[161]. In their approach, they designed a reversible self-folding pNIPAM-AAc and PPF bilayer soft microgrippers with  $\text{Fe}_2\text{O}_3$  and they proved the concept of being used in surgical conditions by the experiment of gripping cells, shown in Figure 19b-ii.

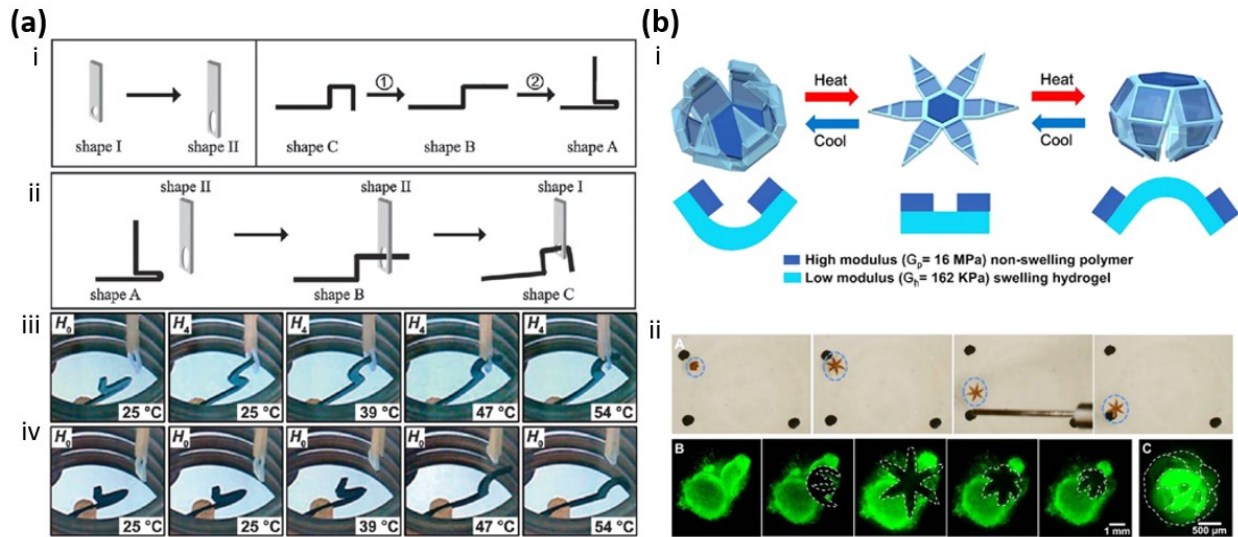


Figure 19. (a) Shape memory of magnetic hydrogels under different heating conditions. (i) actuation of two different programmed samples; (ii) Working principle of the fixation device; (iii) images of sample actuation under environmental heating with magnetic field of 20.2 kA m<sup>-1</sup>; (iv) images of sample actuation under environmental heating only. Reproduced with permission from [158].(b) (i) Configuration of the bilayer hydrogels; (ii) gripping cell experiment under magnetic actuation. Reproduced with permission from [161].

Recent studies in magnetic hydrogel has also considered innovation of the fabrication methods. Nuzzo and his group[162] designed a 3D printed hydrogel with embedded Fe<sub>3</sub>O<sub>4</sub> MNPs to achieve responsiveness to the external magnetic field and the overall system was described as 4D structure. With the technique from 3D printing, they successfully attempted to vary the shape of the hydrogels, which mimic different types of sea jelly organisms. When exposed to the external field of 130mT m<sup>-1</sup>, the object can accelerate to 4mm s<sup>-1</sup> over a 23cm distance, demonstrating the ability to function as an actuator. In addition, they also conducted a series of experiments focusing on the crosslinking gradient localization in order to mimic the dynamic movement of

the organisms. In another study, Xuanhe Zhao and his group [163] designed a submillimeter-scale soft continuum robot, which composed of a soft polymer matrix (PDMS and TPU) with embedded ferromagnetic particles and a layer of hydrophilic hydrogel coating. This robot has the capability of steering and navigation responding to magnetic actuation. Their result showed the thread-like robot being guided through a set of rings and even a life-size 3D cerebrovascular phantom network model. This actuator will aim for clearing the blood clots in vessels, which also further functionalized with delivering drugs or laser light to break up the blockages.

#### ***4.3.3 Magnetic Actuation in Hydrogels Verses Other Actuation Methods***

The actuation of hydrogels can be controlled by many types of stimuli. Table 1 listed the different methods of actuating hydrogels including temperature, pH, light, electric field and magnetic field. Table 1 listed a couple of studies in these fields as well as the previously mentioned studies on magnetic hydrogel actuators.

Hydrogels activated by temperature exhibits reversible change of solubility given different temperatures. Most of these gels are LCST-type, which will experience phase separation (gel collapses) upon heating over the cloud point temperature  $T_c$ . In this way, the hydrogel will contract and there will a decrease in volume. Other hydrogels showing reverse behavior are based on UCST-type polymers, such as polysulfobetaines[164]. With temperature increasing, these hydrogels will expand.

For light-responsive hydrogels, the working mechanism is similar. Since light induces heat, theoretically, any temperature-responsive hydrogels can be activated with light as well. Light actuation shows advantages in many areas such as non-invasive applications. However, due to

the low energy conversion from light to heat, this activation will not be as effective as thermal change as proven by a study of Chu et al. [165].

pH-sensitive hydrogels actuator is also based on the solubility change behavior. For polyelectrolyte hydrogels, such as poly(acrylic acid), the charge density on the chains can be changed reversibly given different solvent with different pH. It will result in swelling and deswelling change so that an actuation by pH is achieved.

As for hydrogels activated by electric field, bending is the common movement which occurs when hydrogels are placed in between two electrodes. For polyelectrolyte hydrogels, the ions will move guided by the electric field that results in a local pH gradient.[166] Therefore, the shrinking and swelling will happen respectively at two sides of the hydrogels and leads to the bending. Actuation by electric field is favored for precise control, the amount of variables and remote control.

For magnetic-induced actuators, their strengths also lie in remote control. Since the actuation response to the field is almost instant, few reported the response time regarding the magnetically controlled actuators. A variation of movements types including stretching and bending can be realized. Overall, it remains great potential in the actuator world.

Table 1. List of Studies of Different Actuation Methods of Hydrogels

<b>Active layer Hydrogels</b>	<b>Types of Stimuli</b>	<b>Activation</b>	<b>Maximum Distortion</b>	<b>Actuation Time</b>	<b>Sample Size</b>	<b>References</b>
P(NIPAM-ABP)	Temperature	4°C - 40°C	Volume change: 680%	<1 s	25mm (diameter) *	[167]

					5mm (thickness)	
Poly(N-isopropylacrylamide)/graphene oxide (PNIPAM-GO)	Temperature	15°C - 45°C	Volume change: 6900%	10 min	~15mm (diameter) *  5mm (thickness)	[165]
Poly(N-isopropylacrylamide-co-acrylic acid) (pNIPAM-AAc)	Temperature	28°C - 43°C	Grippers fully closed at one side to grippers  fully closed at the other side.	On the order of minutes	~2mm *  2mm *  15um	[168]
PNIPAM-GO	Light	NIR light (15°C - 45°C)	Volume change: ~3300%	20 min	~12mm (diameter) *  4mm (thickness)	[165]

Poly(AAc-co-AAm)	pH	4.00pH - 4.25pH	Volume change: ~900%	1 min	10 $\mu$ m * 1.2 $\mu$ m * 11 $\mu$ m	[169]
DMA-containing hydrogels (with deposited Fe <sup>3+</sup> )	pH	7.4 pH - 9.5 pH	Radius of curvature: 0.30 $\pm$ 0.037 mm <sup>-1</sup> increased to 0.41 $\pm$ 0.094 mm <sup>-1</sup>	120 min	20mm * 5mm * 0.7mm	[170]
polyampholyte (PA) hydrogel	Organic Solvents	DI water-- tetrahydrofuran (THF)	Bending angle: ~ 46° Actuation stress: 39.1 G $\pm$ 18.2 kJ/m <sup>3</sup>	>10min to the maximum state	10cm * 10cm * 2.6mm	[171]
Graphene/gelatin hydrogel containing anionic surfactant	Electric Field	0 - 800 V/mm	Highest storage modulus response $\Delta G'$ = 1.25 * 10 <sup>6</sup> Pa	15min	1.39mm (thickness)	[172]

Polyelectrolyte hydrogels (AAm/AMP S/F127DA)	Electric Field	0 - 357 V/m	Bending angle: 110°	120s	50 mm × 2 mm × 1.5 mm	[173]
Vinyl-terminated nano-magnets and the 2-hydroxyethyl methacrylate	Magnetic Field	0 - 0.53 T	Stretched 123% of initial length	N/A	2cm (diameter) * 4.5cm (length)	[153]
Fe <sub>3</sub> O <sub>4</sub> @Fe-alginate/polyacrylamide	Magnetic Field	NdFeB alloy magnet	Stretched 1100% of initial length	N/A	10mm (length) * 6mm (diameter)	[152]
NdFeB particles embedded in PDMS or TPU, coated with	Magnetic Field	5 to 60mT generated by a pair of Helmholtz coils (10cm diameter)	Bending angle: 90°	N/A	600μm (diameter)	[163]

polydimethyl acrylamide (PDMAA) hydrogel						
---	--	--	--	--	--	--

Magnetic hydrogel is rapidly developing field with a lot of promising application possibilities in soft robotics area. Future work on this subject will be continuing improving the mechanical properties, magnetic responsiveness and incorporations with other techniques or specialities such as 3D printing or self-healing for better designs. Magnetic hydrogel is one of the most important members in the soft robotics family especially when it comes to aquatic robots, and it will be applied and benefits the whole soft robotics industry in the near future.

## Chapter 5. Conclusion

This work attempted to develop a novel application of colloidal  $\text{Fe}_3\text{O}_4@\text{SiO}_2$  MNPs as an overpotential alarm device for the battery and review on the recent progress of magnetic hydrogels applications, especially in soft robotics. For the former project, we successfully synthesized the  $\text{Fe}_3\text{O}_4$  magnetic core and coat the surface with a layer of  $\text{SiO}_2$  shell to achieve an improved performance of the nanoparticles. With investigation of the amorphous structure which the nanoparticles assembled into under electric field, we utilized this property to further develop it into a colorimetric voltmeter device. Furthermore, we demonstrated the application with a zinc-air solid state battery and acquired reliable and positive results. For the second study, we started from the different mechanisms which incorporate the MNPs with the hydrogel network. We reviewed some popular areas that magnetic hydrogels are extensively used in, including drug delivery, enzyme immobilization, cell and protein separation, detection and purification in wastewater treatment. We later focused on the magnetic hydrogel applications in the soft robotics field and discussed the challenges and future work related to this area.

Start with Chapter 1, the basic magnetism mechanism and the effects of nanoparticle size on the property change were discussed. The outline of the studies in colloidal MNPs and magnetic hydrogels has been proposed. Current fabrication methods of MNPs, specifically  $\text{Fe}_3\text{O}_4$ , were reviewed and a summary of application areas of  $\text{Fe}_3\text{O}_4$  nanoparticles was mentioned, among which magnetic fluid and magnetic hydrogels have increasingly great potentials.

Chapter 2 provided background information for the later chapter, mainly on colloidal nanoparticles under electric field and the introduction of amorphous photonic crystal structure. For the first part, nanoparticles being stabilized with the double layer structure in solution was

described, followed by the electrophoretic movement of the particles under electric field. The basic schematic structure of the nanoparticles arrangement under this condition was demonstrated after that, which led to our discussion on the photonic structure in the second part. With an introduction of the origins of structural color, conventional photonic crystal and amorphous photonic crystal structures were discussed and compared in many aspects such as the properties of the reflected light and bandgap difference. In addition, methods of creating these structures were summarized, where electric field-assisted self-assembly process was highlighted as a precious and facile way to tune the structural color dynamically. These information formed the basis of our experimental works in the later chapters.

Chapter 3 focused on colloidal MNPs fabrication and the application as an overpotential alarm system. The materials, synthesis procedures, characterization methods, analysis of the and the application demonstration were covered. The list of materials and the details of preliminary preparation was mentioned. The synthesis of  $\text{Fe}_3\text{O}_4$  MNPs by solvothermal method was discussed in detail as well as the Stöber method of  $\text{SiO}_2$  coating process. The colorimetric voltmeter device was also fabricated by the nanoparticle solution and two ITO plates. Zinc-air solid-state battery with PVA-KOH as polyelectrolyte was prepared and the whole monitoring system was assembled with the help of designed acrylic mold. Besides synthesis, characterization methods of both the nanoparticles and the device were put forward including zeta potential, XRD, SEM, DLS measurements and cyclic tests for the battery performance. For the results,  $\text{Fe}_3\text{O}_4$  nanoparticles and  $\text{Fe}_3\text{O}_4 @\text{SiO}_2$  nanoparticles were brought into comparison regarding the different results gained from zeta potential, XRD, SEM, DLS characterization respectively. Based on the discussion, it was clear that the property of colloidal stability, surface morphology, nanoparticle size distribution had been positively improved due to  $\text{SiO}_2$  shell. With

the color information obtained from the images of the colorimetric monitoring device, digital analysis was conducted and transform the information into a reliable parameter hue. The hue values were also plotted with voltage and viewing angles respectively, showing that the color was angle-independent but highly dependent on the electric field intensity and it can response to the potential change with a satisfactory precision. Furthermore, we measured the battery performances under two conditions, either with or without the device attached. The results showed little difference between the results, so it further confirmed our idea of creating a non-burden voltmeter device. Illustrated by a graph of four battery behaviours, which are discharging, charging, overcharging and aging, we demonstrated the prominent color change of the device during these four stages. In this way, we can monitor the battery by using our nanoparticle device based on its color.

Chapter 4 drew attention to the current progress of MNPs in hydrogels and their various types of applications, typically in soft robotics. Three different mechanisms of how nanoparticles existed in the hydrogels were discussed and illustrated, including the blending, in situ precipitation and grafting-onto methods. Traditional fields of magnetic hydrogels such as drug delivery, enzyme immobilization, cell and protein separation, detection and purification in wastewater treatment were reviewed with examples from the literature. The final part was focus on how magnetic hydrogels could be a significant member of the soft robotics family. The advantages of high elasticity and stretchability along with other desirable mechanical properties of the hydrogels were combined with the noncontact magnetic responsiveness of MNPs. Two major functioning mechanism were discussed as directly responsive to the external field mechanically or through magnetothermal effect. For both materials, examples were given to demonstrated how they could deform (including elongation, coiling, torsion, rotation and bending) under different types of

external magnetic fields and be used in actuators, biomimicking robots and etc.. The challenge of maintaining the mechanism elasticity and toughness while increasing the magnetic responsiveness to the applied field is also put forward, with an example approach to tackle the problem. A table listed several example works of magnetic responsive hydrogel as an important member in the actuator family, along with other actuators including temperature, pH, light, electric field were put out and discussed. Future work better improving the materials performance and incorporating new technologies such as 3D In-jet printing could be looked forward to.

Overall, MNPs have great advantage and potentials to be applied in both colloid and hydrogel based smart materials. Future works of applications can be focused on digging more into the current developing fields or further expanding into other new field combing strengths of other materials. The former case may include the steering and navigating assistance of MNPs especially in drug delivery in vessels, clearing clots in different organs[163], stimulating nerves reactions[174] in biomedical fields. For certain medical tests, such as gastroscopy[175], patient needs to swallow chemicals as for assisting the imaging. MNPs can be designed as attaching to the chemicals so that the substance can be collected back. The ability of MNPs in large quantity being attracted and sedimented could be also used to absorb air pollutants particles for air purification. As for the latter case, which needs more innovated ideas to relate MNPs to new fields, applications of artificial muscles for human being or even for other creatures[176] can be possible developed using magnetic actuation. It is anticipated that these fields of MNPs will continue to grow, and applications related to these fields will be beneficial to the future of human welfare.

## Reference

1. Pankhurst, Q.A., et al., *Applications of magnetic nanoparticles in biomedicine*. Journal of physics D: Applied physics, 2003. **36**(13): p. R167.
2. Souza, G.R., et al., *Magnetic Nanoparticles for 3D Cell Culture*, in *Nanomagnetic Actuation in Biomedicine*. 2018, CRC Press. p. 241-256.
3. Mornet, S., et al., *Magnetic nanoparticle design for medical applications*. Progress in Solid State Chemistry, 2006. **34**(2-4): p. 237-247.
4. Yang, H.-M., et al., *Cross-linked magnetic nanoparticles with a biocompatible amide bond for cancer-targeted dual optical/magnetic resonance imaging*. 2018. **161**: p. 183-191.
5. Ramaswamy, B., et al., *Movement of magnetic nanoparticles in brain tissue: mechanisms and impact on normal neuronal function*. Nanomedicine: Nanotechnology, Biology and Medicine, 2015. **11**(7): p. 1821-1829.
6. Kim, J.S., et al., *Toxicity and tissue distribution of magnetic nanoparticles in mice*. Toxicological Sciences, 2005. **89**(1): p. 338-347.
7. Vangijzegem, T., D. Stanicki, and S.J.E.o.o.d.d. Laurent, *Magnetic iron oxide nanoparticles for drug delivery: applications and characteristics*. 2019. **16**(1): p. 69-78.
8. Elliott, D.W. and W.-X. Zhang, *Field assessment of nanoscale bimetallic particles for groundwater treatment*. Environmental Science & Technology, 2001. **35**(24): p. 4922-4926.
9. Ngomsik, A.-F., et al., *Magnetic nano- and microparticles for metal removal and environmental applications: a review*. Comptes Rendus Chimie, 2005. **8**(6-7): p. 963-970.
10. Sanchez, L.M., et al., *Effect of PAA-coated magnetic nanoparticles on the performance of PVA-based hydrogels developed to be used as environmental remediation devices*. 2019. **21**(3): p. 64.
11. Kavre, I., et al., *Fabrication of magneto-responsive microgears based on magnetic nanoparticle embedded PDMS*. RSC advances, 2014. **4**(72): p. 38316-38322.
12. Mahendran, V. and J. Philip, *Nanofluid based optical sensor for rapid visual inspection of defects in ferromagnetic materials*. Applied Physics Letters, 2012. **100**(7): p. 073104.
13. He, L., et al., *Magnetic assembly route to colloidal responsive photonic nanostructures*. Accounts of chemical research, 2012. **45**(9): p. 1431-1440.
14. Ge, J., Y. Hu, and Y. Yin, *Highly tunable superparamagnetic colloidal photonic crystals*. Angewandte Chemie International Edition, 2007. **46**(39): p. 7428-7431.
15. Lu, X., et al., *Highly charged, magnetically sensitive magnetite/polystyrene colloids: synthesis and tunable optical properties*. 2019. **54**(10): p. 7628-7636.
16. Jacobson, J.M., et al., *Electrophoretic displays using nanoparticles*. 2003, Google Patents.
17. Frau, E. and S. Schintke. *Modulated 3D cross-correlation dynamic light scattering of magnetic nanoparticle inks*. in *2018 20th International Conference on Transparent Optical Networks (ICTON)*. 2018. IEEE.
18. Christian, P., et al., *Nanoparticles: structure, properties, preparation and behaviour in environmental media*. Ecotoxicology, 2008. **17**(5): p. 326-343.
19. Yang, W., J.I. Peters, and R.O. Williams III, *Inhaled nanoparticles—a current review*. International journal of pharmaceutics, 2008. **356**(1-2): p. 239-247.
20. Sun, J., et al., *Synthesis and characterization of biocompatible Fe<sub>3</sub>O<sub>4</sub> nanoparticles*. 2007. **80**(2): p. 333-341.
21. Gupta, A.K. and S.J.I.t.o.n. Wells, *Surface-modified superparamagnetic nanoparticles for drug delivery: preparation, characterization, and cytotoxicity studies*. 2004. **3**(1): p. 66-73.

22. Jeong, U., et al., *Superparamagnetic colloids: controlled synthesis and niche applications*. 2007. **19**(1): p. 33-60.
23. O'Handley, R.C., *Soft magnetic materials*. Mod Magn Mater, 2000. **29**: p. 198.
24. Stoner, E.C. and E. Wohlfarth, *A mechanism of magnetic hysteresis in heterogeneous alloys*. Philosophical Transactions of the Royal Society of London. Series A, Mathematical and Physical Sciences, 1948. **240**(826): p. 599-642.
25. Majetich, S.A., T. Wen, and O.T. Mefford, *Magnetic nanoparticles*. MRS Bulletin, 2013. **38**(11): p. 899-903.
26. Odenbach, S., *Recent progress in magnetic fluid research*. Journal of physics: condensed matter, 2004. **16**(32): p. R1135.
27. Nkurikiyimfura, I., Y. Wang, and Z. Pan, *Heat transfer enhancement by magnetic nanofluids—a review*. Renewable and Sustainable Energy Reviews, 2013. **21**: p. 548-561.
28. Helgeland, W., *Magnetic fluid sealing device*. 1998, Google Patents.
29. Svoboda, J. and T. Fujita, *Recent developments in magnetic methods of material separation*. Minerals Engineering, 2003. **16**(9): p. 785-792.
30. Haider, H., et al., *Exceptionally tough and notch-insensitive magnetic hydrogels*. Soft Matter, 2015. **11**(42): p. 8253-8261.
31. Tamez Jr, C., *Remediation of copper (II) and lead (II) from aqueous solution using engineered iron oxide and manganese oxide nanomaterials*. 2013: The University of Texas-Pan American.
32. Li, Z., Q. Sun, and M. Gao, *Preparation of water-soluble magnetite nanocrystals from hydrated ferric salts in 2-pyrrolidone: mechanism leading to Fe<sub>3</sub>O<sub>4</sub>*. Angewandte Chemie International Edition, 2005. **44**(1): p. 123-126.
33. Gao, S., et al., *Biopolymer-assisted green synthesis of iron oxide nanoparticles and their magnetic properties*. The Journal of Physical Chemistry C, 2008. **112**(28): p. 10398-10401.
34. Li, J., Q. Wu, and J. Wu, *Synthesis of nanoparticles via solvothermal and hydrothermal methods*. Handbook of Nanoparticles, 2016: p. 295-328.
35. YU, S.-H., *Hydrothermal/solvothermal processing of advanced ceramic materials*. Journal of the Ceramic Society of Japan, 2001. **109**(1269): p. S65-S75.
36. Pinna, N., et al., *Magnetite nanocrystals: nonaqueous synthesis, characterization, and solubility*. Chemistry of Materials, 2005. **17**(11): p. 3044-3049.
37. Indira, T. and P. Lakshmi, *Magnetic nanoparticles—a review*. Int. J. Pharm. Sci. Nanotechnol, 2010. **3**(3): p. 1035-1042.
38. Kim, D., et al., *Surface-modified magnetite nanoparticles for hyperthermia: Preparation, characterization, and cytotoxicity studies*. Current Applied Physics, 2006. **6**: p. e242-e246.
39. Zhi, J., et al., *In situ preparation of magnetic chitosan/Fe<sub>3</sub>O<sub>4</sub> composite nanoparticles in tiny pools of water-in-oil microemulsion*. Reactive and Functional Polymers, 2006. **66**(12): p. 1552-1558.
40. Patsula, V., et al., *Superparamagnetic Fe<sub>3</sub>O<sub>4</sub> nanoparticles: synthesis by thermal decomposition of iron (III) glucuronate and application in magnetic resonance imaging*. ACS applied materials & interfaces, 2016. **8**(11): p. 7238-7247.
41. Wanna, Y., et al., *Efficiency of SPIONs functionalized with polyethylene glycol bis (amine) for heavy metal removal*. Journal of Magnetism and Magnetic Materials, 2016. **414**: p. 32-37.
42. Shen, Y., et al., *Tailoring size and structural distortion of Fe<sub>3</sub>O<sub>4</sub> nanoparticles for the purification of contaminated water*. Bioresource technology, 2009. **100**(18): p. 4139-4146.
43. Brollo, M., et al., *Magnetic hyperthermia in brick-like Ag@ Fe<sub>3</sub>O<sub>4</sub> core-shell nanoparticles*. Journal of Magnetism and Magnetic Materials, 2016. **397**: p. 20-27.

44. Johannsen, M., et al., *Magnetic nanoparticle hyperthermia for prostate cancer*. International Journal of Hyperthermia, 2010. **26**(8): p. 790-795.
45. Nazli, C., et al., *Targeted delivery of doxorubicin into tumor cells via MMP-sensitive PEG hydrogel-coated magnetic iron oxide nanoparticles (MIONPs)*. Colloids and Surfaces B: Biointerfaces, 2014. **122**: p. 674-683.
46. Shinkai, M., et al., *Antibody-conjugated magnetoliposomes for targeting cancer cells and their application in hyperthermia*. Biotechnology and applied biochemistry, 1995. **21**(2): p. 125-137.
47. Hong, C.-Y., et al., *Ordered structures in Fe<sub>3</sub>O<sub>4</sub> kerosene-based ferrofluids*. Journal of applied physics, 1997. **81**(8): p. 4275-4277.
48. Tsuda, S., *Micro-speaker and method for assembling a micro-speaker*. 2004, Google Patents.
49. Raj, K. and R. Moskowitz, *Commercial applications of ferrofluids*. Journal of Magnetism and Magnetic Materials, 1990. **85**(1-3): p. 233-245.
50. King, J.A., *Method for making loudspeaker with magnetic fluid enveloping the voice coil*. 1977, Google Patents.
51. Marinică, O., et al., *Nano-micro composite magnetic fluids: Magnetic and magnetorheological evaluation for rotating seal and vibration damper applications*. Journal of Magnetism and Magnetic Materials, 2016. **406**: p. 134-143.
52. Ge, J. and Y. Yin, *Magnetically tunable colloidal photonic structures in alkanol solutions*. Advanced materials, 2008. **20**(18): p. 3485-3491.
53. Yu, C.-H., K. Tam, and E.S.J.H.o.M.P. Tsang, *Chemical methods for preparation of nanoparticles in solution*. 2008. **5**: p. 113-141.
54. Dahman, Y., *Nanotechnology and Functional Materials for Engineers*. 2017: Elsevier.
55. Besra, L. and M. Liu, *A review on fundamentals and applications of electrophoretic deposition (EPD)*. Progress in materials science, 2007. **52**(1): p. 1-61.
56. Stern, O., *Zur theorie der elektrolytischen doppelschicht*. Zeitschrift für Elektrochemie und angewandte physikalische Chemie, 1924. **30**(21-22): p. 508-516.
57. Hunter, R.J., *Zeta potential in colloid science: principles and applications*. Vol. 2. 2013: Academic press.
58. Lyklema, J., *Fundamentals of interface and colloid science. Volume 2: Solid-liquid interfaces. With special contributions by A. de Keizer, BH Bijsterbosch, GJ Fleer and MA Cohen Stuart*. 1995.
59. Hunter, R.J., *Foundations of colloid science*. 2001: Oxford university press.
60. Lee, E., *Theory of Electrophoresis and Diffusiophoresis of Highly Charged Colloidal Particles*. Vol. 26. 2018: Academic Press.
61. Henry, D., *The cataphoresis of suspended particles. Part I.—The equation of cataphoresis*. Proceedings of the Royal Society of London. Series A, Containing Papers of a Mathematical and Physical Character, 1931. **133**(821): p. 106-129.
62. Clogston, J.D. and A.K. Patri, *Zeta potential measurement*, in *Characterization of nanoparticles intended for drug delivery*. 2011, Springer. p. 63-70.
63. Shim, T.S., et al., *Dynamic modulation of photonic bandgaps in crystalline colloidal arrays under electric field*. Advanced Materials, 2010. **22**(40): p. 4494-4498.
64. Ge, D., et al., *Spray coating of superhydrophobic and angle-independent coloured films*. Chemical Communications, 2014. **50**(19): p. 2469-2472.
65. Takeoka, Y., *Angle-independent structural coloured amorphous arrays*. Journal of Materials Chemistry, 2012. **22**(44): p. 23299-23309.
66. Xu, D., et al., *Thermoresponsive photonic crystal: synergistic effect of poly (N-isopropylacrylamide)-co-acrylic acid and morpho butterfly wing*. ACS applied materials & interfaces, 2015. **7**(16): p. 8750-8756.

67. Prum, R.O., et al., *Coherent light scattering by nanostructured collagen arrays in the caruncles of the Malagasy asities (Eurylaimidae: Aves)*. Journal of Experimental Biology, 1999. **202**(24): p. 3507-3522.
68. Lord, R. *Studies of iridescent colour, and the structure producing it. IV Iridescent beetles* R. Soc. in Proc. 1923.
69. Michelson, A.A., *LXI. On metallic colouring in birds and insects*. The London, Edinburgh, and Dublin Philosophical Magazine and Journal of Science, 1911. **21**(124): p. 554-567.
70. Rayleigh, L., *VII. On the optical character of some brilliant animal colours*. The London, Edinburgh, and Dublin Philosophical Magazine and Journal of Science, 1919. **37**(217): p. 98-111.
71. Onslow, H., *I.—On a periodic structure in many insect scales, and the cause of their iridescent colours*. Philosophical Transactions of the Royal Society of London. Series B, Containing Papers of a Biological Character, 1923. **211**(382-390): p. 1-74.
72. Merritt, E., *A Spectrophotometric Study of Certain Cases of Structural Color*. JOSA, 1925. **11**(2): p. 93-98.
73. Mason, C.W., *Structural colors in insects. I*. The Journal of Physical Chemistry, 1926. **30**(3): p. 383-395.
74. Ge, J. and Y. Yin, *Responsive photonic crystals*. Angewandte Chemie International Edition, 2011. **50**(7): p. 1492-1522.
75. Bucher, M. and D.P. Siemens, *Unified diagram for Fraunhofer diffraction and interference patterns from single, double, and multiple slits*. American Journal of Physics, 1989. **57**(10): p. 902-907.
76. Nie, S. and S.R. Emory, *Probing single molecules and single nanoparticles by surface-enhanced Raman scattering*. science, 1997. **275**(5303): p. 1102-1106.
77. Shi, L., et al., *Amorphous Photonic Crystals with Only Short-Range Order*. Advanced Materials, 2013. **25**(37): p. 5314-5320.
78. John, S., *Strong localization of photons in certain disordered dielectric superlattices*. Physical review letters, 1987. **58**(23): p. 2486.
79. Yablonovitch, E., *Inhibited spontaneous emission in solid-state physics and electronics*. Physical review letters, 1987. **58**(20): p. 2059.
80. Joannopoulos, J.D., et al., *Molding the flow of light*. Princeton Univ. Press, Princeton, NJ [ua], 2008.
81. Mancin, F., et al., *Self-assembled fluorescent chemosensors*. Chemistry—A European Journal, 2006. **12**(7): p. 1844-1854.
82. Bibette, J., *Monodisperse ferrofluid emulsions*. Journal of magnetism and magnetic materials, 1993. **122**(1-3): p. 37-41.
83. Xu, X., et al., *Superparamagnetic photonic crystals*. Advanced materials, 2001. **13**(22): p. 1681-1684.
84. Yin, H., et al., *Amorphous diamond-structured photonic crystal in the feather barbs of the scarlet macaw*. Proceedings of the National Academy of Sciences, 2012. **109**(27): p. 10798-10801.
85. Takeoka, Y.J.J.o.M.C., *Angle-independent structural coloured amorphous arrays*. 2012. **22**(44): p. 23299-23309.
86. Raman, C.V. *The Indian musical drums*. in *Proceedings of the Indian Academy of Sciences-Section A*. 1934. Springer.
87. Dyck, J.J.B.S., *Structure and spectral reflectance of green and blue feathers of the rose-faced lovebird (Agapornis roseicollis)*. 1971. **18**(2): p. 1-67.
88. Prum, R.O., et al., *Coherent light scattering by blue feather barbs*. 1998. **396**(6706): p. 28.

89. Joannopoulos, J.D., R.D. Meade, and J. Winn, *Photonic Crystals-Molding the flow of light.*(1995). Appendix D, PRINCETON, 1997.
90. Dong, B., et al., *Structural coloration and photonic pseudogap in natural random close-packing photonic structures.* Optics express, 2010. **18**(14): p. 14430-14438.
91. Taflove, A. and S.C. Hagness, *Computational electrodynamics: the finite-difference time-domain method.* 2005: Artech house.
92. Jodrey, W. and E. Tory, *Computer simulation of close random packing of equal spheres.* Physical review A, 1985. **32**(4): p. 2347.
93. Edagawa, K., S. Kanoko, and M. Notomi, *Photonic amorphous diamond structure with a 3D photonic band gap.* Physical review letters, 2008. **100**(1): p. 013901.
94. Forster, J.D., et al., *Biomimetic isotropic nanostructures for structural coloration.* Advanced Materials, 2010. **22**(26-27): p. 2939-2944.
95. Lee, I., et al., *Quasi-amorphous colloidal structures for electrically tunable full-color photonic pixels with angle-independency.* Advanced Materials, 2010. **22**(44): p. 4973-4977.
96. Fenzl, C., T. Hirsch, and O.S. Wolfbeis, *Photonic crystals for chemical sensing and biosensing.* Angewandte Chemie International Edition, 2014. **53**(13): p. 3318-3335.
97. Zhang, J.-T., et al., *2-D array photonic crystal sensing motif.* Journal of the American Chemical Society, 2011. **133**(24): p. 9152-9155.
98. Vukusic, P. and J.R. Sambles, *Photonic structures in biology.* Nature, 2003. **424**(6950): p. 852.
99. Joannopoulos, J., et al., *Photonic Crystals: Molding the Flow of Light 2nd edn Princeton Univ.* 2008, Press.
100. Yue, Y. and J.P. Gong, *Tunable one-dimensional photonic crystals from soft materials.* Journal of Photochemistry and Photobiology C: Photochemistry Reviews, 2015. **23**: p. 45-67.
101. Liu, X.Y., *Bioinspiration: from nano to micro scales.* 2012: Springer.
102. Maldovan, M. and E.L. Thomas, *Diamond-structured photonic crystals.* Nature materials, 2004. **3**(9): p. 593.
103. Xu, W., Z. Li, and Y. Yin, *Colloidal Assembly Approaches to Micro/Nanostructures of Complex Morphologies.* Small, 2018. **14**(35): p. 1801083.
104. Wei, Y., et al., *Synthesis of Fe<sub>3</sub>O<sub>4</sub> nanoparticles and their magnetic properties.* Procedia Engineering, 2012. **27**: p. 632-637.
105. Farimani, M.H.R., et al., *Study of structural and magnetic properties of superparamagnetic Fe<sub>3</sub>O<sub>4</sub>/SiO<sub>2</sub> core-shell nanocomposites synthesized with hydrophilic citrate-modified Fe<sub>3</sub>O<sub>4</sub> seeds via a sol-gel approach.* Physica E: Low-dimensional Systems and Nanostructures, 2013. **53**: p. 207-216.
106. Stöber, W., A. Fink, and E. Bohn, *Controlled growth of monodisperse silica spheres in the micron size range.* Journal of colloid and interface science, 1968. **26**(1): p. 62-69.
107. Wang, H., et al., *Effect of solvents on the preparation of silica-coated magnetic particles.* Chemistry letters, 2001. **30**(11): p. 1168-1169.
108. Deng, Y.-H., et al., *Investigation of formation of silica-coated magnetite nanoparticles via sol-gel approach.* Colloids and Surfaces A: Physicochemical and Engineering Aspects, 2005. **262**(1-3): p. 87-93.
109. Chang, Q., et al., *Synthesis and properties of magnetic and luminescent Fe<sub>3</sub>O<sub>4</sub>/SiO<sub>2</sub>/Dye/SiO<sub>2</sub> nanoparticles.* Journal of Luminescence, 2008. **128**(12): p. 1890-1895.
110. Haw, C., et al., *Morphological studies of randomized dispersion magnetite nanoclusters coated with silica.* Ceramics International, 2011. **37**(2): p. 451-464.

111. Dong, F., et al., *Highly Porous, Water-Soluble, Superparamagnetic, and Biocompatible Magnetite Nanocrystal Clusters for Targeted Drug Delivery*. Chemistry—A European Journal, 2011. **17**(45): p. 12802-12808.
112. Kawamura, A., et al., *Full-color biomimetic photonic materials with iridescent and non-iridescent structural colors*. Scientific reports, 2016. **6**: p. 33984.
113. Nucara, L., F. Greco, and V. Mattoli, *Electrically responsive photonic crystals: a review*. Journal of Materials Chemistry C, 2015. **3**(33): p. 8449-8467.
114. Han, M.G., et al., *Electrically tunable photonic crystals from long-range ordered crystalline arrays composed of copolymer colloids*. Journal of Materials Chemistry C, 2013. **1**(36): p. 5791-5798.
115. Luo, Y., et al., *Electric field induced structural color changes of SiO<sub>2</sub>@TiO<sub>2</sub> core-shell colloidal suspensions*. Journal of Materials Chemistry C, 2014. **2**(11): p. 1990-1994.
116. Shim, H., et al., *Spectral reflectance switching of colloidal photonic crystal structure composed of positively charged TiO<sub>2</sub> nanoparticles*. Applied Physics Letters, 2012. **100**(6): p. 063113.
117. Wang, W., et al., *Large-scale preparation of size-controlled Fe<sub>3</sub>O<sub>4</sub>@SiO<sub>2</sub> particles for electrophoretic display with non-iridescent structural colors*. RSC advances, 2019. **9**(1): p. 498-506.
118. Girishkumar, G., et al., *Lithium-air battery: promise and challenges*. The Journal of Physical Chemistry Letters, 2010. **1**(14): p. 2193-2203.
119. Blurton, K.F. and A.F. Sammells, *Metal/air batteries: their status and potential—a review*. Journal of Power Sources, 1979. **4**(4): p. 263-279.
120. Pei, P., K. Wang, and Z. Ma, *Technologies for extending zinc-air battery's cyclelife: A review*. Applied Energy, 2014. **128**: p. 315-324.
121. Jarosz, A.M. and R.R. Stevens, *Portable combination lamp, smoke detector and power failure alarm*. 1983, Google Patents.
122. Fridman, R., *Battery monitoring system*. 1989, Google Patents.
123. MacIntyre, H.L., I.R.D. Graham, and M.B. Aldava, *Battery monitoring system of cell groups and display*. 1990, Google Patents.
124. Lee, J.S., et al., *Metal-air batteries with high energy density: Li-air versus Zn-air*. Advanced Energy Materials, 2011. **1**(1): p. 34-50.
125. Marković, N., et al., *Oxygen reduction reaction on Pt and Pt bimetallic surfaces: a selective review*. Fuel cells, 2001. **1**(2): p. 105-116.
126. Reier, T., M. Oezaslan, and P. Strasser, *Electrocatalytic oxygen evolution reaction (OER) on Ru, Ir, and Pt catalysts: a comparative study of nanoparticles and bulk materials*. ACS Catalysis, 2012. **2**(8): p. 1765-1772.
127. Li, B., et al., *Alkaline poly(vinyl alcohol)/poly(acrylic acid) polymer electrolyte membrane for Ni-MH battery application*. Ionics, 2015. **21**(1): p. 141-148.
128. Grumezescu, A.M., *Multifunctional systems for combined delivery, biosensing and diagnostics*. 2017: William Andrew.
129. Gholami, T., et al., *Synthesis and characterization of spherical silica nanoparticles by modified Stöber process assisted by organic ligand*. Superlattices and Microstructures, 2013. **61**: p. 33-41.
130. Charaya, H., et al., *Thermochromic and Piezocapacitive Flexible Sensor Array by Combining Composite Elastomer Dielectrics and Transparent Ionic Hydrogel Electrodes*. Advanced Materials Technologies, 2019: p. 1900327.
131. Ashforth-Frost, S., *Quantitative thermal imaging using liquid crystals*. Journal of biomedical optics, 1996. **1**(1): p. 18-28.
132. Farina, D.J., et al., *Illuminant invariant calibration of thermochromic liquid crystals*. Experimental thermal and fluid Science, 1994. **9**(1): p. 1-12.

133. Stasiek, J., et al., *Liquid crystal thermography and true-colour digital image processing*. Optics & Laser Technology, 2006. **38**(4-6): p. 243-256.
134. Chan, C., Q. Yu, and K. Ho, *Order-N spectral method for electromagnetic waves*. Physical Review B, 1995. **51**(23): p. 16635.
135. Li, Y. and H. Dai, *Recent advances in zinc-air batteries*. Chemical Society Reviews, 2014. **43**(15): p. 5257-5275.
136. Tran, T.N.T.C., M. P.; Chung, H. J.; Ivey, D. G., , *Effect of Cross-Linker Concentration in Polymer Network on performance of Zinc-Air Batteries*. Batteries & Supercaps 2019.
137. Wang, Q., et al., *Amphiphilic dextran/magnetite nanocomposites as magnetic resonance imaging probes*. Chinese science bulletin, 2009. **54**(17): p. 2925-2933.
138. Li, Y., et al., *Magnetic hydrogels and their potential biomedical applications*. Advanced Functional Materials, 2013. **23**(6): p. 660-672.
139. Cho, D.-W., et al., *Natural, synthetic and semi-synthetic polymers*, in *Organ Printing*. 2015, Morgan & Claypool Publishers.
140. Liu, H., et al., *Magnetic hydrogels with supracolloidal structures prepared by suspension polymerization stabilized by Fe<sub>2</sub>O<sub>3</sub> nanoparticles*. Acta biomaterialia, 2010. **6**(1): p. 275-281.
141. Ahmad, H., et al., *Evaluating a simple blending approach to prepare magnetic and stimuli-responsive composite hydrogel particles for application in biomedical field*. Express Polymer Letters, 2016. **10**(8).
142. Tóth, I.Y., et al., *Magnetic hyaluronate hydrogels: preparation and characterization*. Journal of Magnetism and Magnetic Materials, 2015. **380**: p. 175-180.
143. Zhao, W., et al., *In situ synthesis of magnetic field-responsive hemicellulose hydrogels for drug delivery*. Biomacromolecules, 2015. **16**(8): p. 2522-2528.
144. Jiang, L. and P. Liu, *Design of magnetic attapulgitite/fly ash/poly (acrylic acid) ternary nanocomposite hydrogels and performance evaluation as selective adsorbent for Pb<sup>2+</sup> ion*. ACS Sustainable Chemistry & Engineering, 2014. **2**(7): p. 1785-1794.
145. Messing, R., et al., *Cobalt ferrite nanoparticles as multifunctional cross-linkers in PAAm ferrogels*. Macromolecules, 2011. **44**(8): p. 2990-2999.
146. Liu, T.-Y., et al., *Magnetic-sensitive behavior of intelligent ferrogels for controlled release of drug*. Langmuir, 2006. **22**(14): p. 5974-5978.
147. Satarkar, N.S. and J.Z. Hilt, *Magnetic hydrogel nanocomposites for remote controlled pulsatile drug release*. Journal of Controlled Release, 2008. **130**(3): p. 246-251.
148. Hoare, T., et al., *Magnetically triggered nanocomposite membranes: a versatile platform for triggered drug release*. Nano letters, 2011. **11**(3): p. 1395-1400.
149. Tang, S.C., et al., *Synthesis and application of magnetic hydrogel for Cr (VI) removal from contaminated water*. Environmental Engineering Science, 2010. **27**(11): p. 947-954.
150. Satarkar, N.S. and J.Z.J.J.o.C.R. Hilt, *Magnetic hydrogel nanocomposites for remote controlled pulsatile drug release*. 2008. **130**(3): p. 246-251.
151. Liu, T.-Y., et al., *Magnetic-sensitive behavior of intelligent ferrogels for controlled release of drug*. 2006. **22**(14): p. 5974-5978.
152. Haider, H., et al., *Exceptionally tough and notch-insensitive magnetic hydrogels*. 2015. **11**(42): p. 8253-8261.
153. Fuhrer, R., et al., *Crosslinking metal nanoparticles into the polymer backbone of hydrogels enables preparation of soft, magnetic field-driven actuators with muscle-like flexibility*. 2009. **5**(3): p. 383-388.

154. Meng, H. and J. Hu, *A brief review of stimulus-active polymers responsive to thermal, light, magnetic, electric, and water/solvent stimuli*. Journal of Intelligent Material Systems and Structures, 2010. **21**(9): p. 859-885.
155. Szabo, D., G. Szeghy, and M. Zrinyi, *Shape transition of magnetic field sensitive polymer gels*. Macromolecules, 1998. **31**(19): p. 6541-6548.
156. Caykara, T., D. Yörük, and S. Demirci, *Preparation and characterization of poly (N-tert-butylacrylamide-co-acrylamide) ferrogel*. Journal of Applied Polymer Science, 2009. **112**(2): p. 800-804.
157. Fuhrer, R., et al., *Crosslinking metal nanoparticles into the polymer backbone of hydrogels enables preparation of soft, magnetic field-driven actuators with muscle-like flexibility*. Small, 2009. **5**(3): p. 383-388.
158. Kumar, U.N., et al., *Shape-Memory Nanocomposites with Magnetically Adjustable Apparent Switching Temperatures*. Advanced Materials, 2011. **23**(36): p. 4157-4162.
159. Razzaq, M., M. Behl, and A. Lendlein, *Magnetic memory effect of nanocomposites*. Advanced Functional Materials, 2012. **22**(1): p. 184-191.
160. Shen, T., et al., *Remotely triggered locomotion of hydrogel mag-bots in confined spaces*. Scientific reports, 2017. **7**(1): p. 16178.
161. Breger, J.C., et al., *Self-folding thermo-magnetically responsive soft microgrippers*. ACS applied materials & interfaces, 2015. **7**(5): p. 3398-3405.
162. McCracken, J.M., et al., *Ionic Hydrogels with Biomimetic 4D-Printed Mechanical Gradients: Models for Soft-Bodied Aquatic Organisms*. Advanced Functional Materials, 2019: p. 1806723.
163. Kim, Y., et al., *Ferromagnetic soft continuum robots*. 2019. **4**(33): p. eaax7329.
164. Huglin, M.B. and M.A.J.P.i. Radwan, *Unperturbed dimensions of a zwitterionic polymethacrylate*. 1991. **26**(2): p. 97-104.
165. Shi, K., et al., *Near-infrared light-responsive poly (N-isopropylacrylamide)/graphene oxide nanocomposite hydrogels with ultrahigh tensibility*. 2015. **7**(49): p. 27289-27298.
166. Messing, R. and A.M.J.P.C. Schmidt, *Perspectives for the mechanical manipulation of hybrid hydrogels*. 2011. **2**(1): p. 18-32.
167. Jiang, S., et al., *Unusual and superfast temperature-triggered actuators*. 2015. **27**(33): p. 4865-4870.
168. Breger, J.C., et al., *Self-folding thermo-magnetically responsive soft microgrippers*. 2015. **7**(5): p. 3398-3405.
169. Zarzar, L.D., P. Kim, and J.J.A.m. Aizenberg, *Bio-inspired Design of Submerged Hydrogel-Actuated Polymer Microstructures Operating in Response to pH*. 2011. **23**(12): p. 1442-1446.
170. Lee, B.P. and S.J.A.M. Konst, *Novel hydrogel actuator inspired by reversible mussel adhesive protein chemistry*. 2014. **26**(21): p. 3415-3419.
171. Hubbard, A.M., et al., *Hydrogel/Elastomer Laminates Bonded via Fabric Interphases for Stimuli-Responsive Actuators*. 2019.
172. Tungkavet, T., et al., *Graphene/gelatin hydrogel composites with high storage modulus sensitivity for using as electroactive actuator: Effects of surface area and electric field strength*. 2015. **70**: p. 242-251.
173. Li, Y., et al., *Electric field actuation of tough electroactive hydrogels cross-linked by functional triblock copolymer micelles*. 2016. **8**(39): p. 26326-26331.
174. Lee, Y. and T.-W.J.A.o.c.r. Lee, *Organic Synapses for Neuromorphic Electronics: From Brain-Inspired Computing to Sensorimotor Nervetronics*. 2019. **52**(4): p. 964-974.

175. Balogh, B., T. Kovács, and A.K.J.W.J.o.P. Saxena, *Complications in children with percutaneous endoscopic gastrostomy (PEG) placement*. 2019. **15**(1): p. 12-16.
176. Gao, Z., et al., *An overview of biomimetic robots with animal behaviors*. 2019. **332**: p. 339-350.